Nano Research

ISSN 1998-0124 CN 11-5974/O4
https://doi.org/10.1007/s12274-021-3974-y

Review Article

2D layered black arsenic-phosphorus materials: Synthesis, properties, and device applications

Junchuan Liang[1,2,§], Yi Hu[1,2,§], Kaiqiang Zhang[1,2], Yaoda Wang[1,2], Xinmei Song[1,2], Anyang Tao[1,2], Yuzhu Liu[1,2], and Zhong Jin[1,2] (✉)

[1] *MOE Key Laboratory of Mesoscopic Chemistry, MOE Key Laboratory of High Performance Polymer Materials and Technology, Jiangsu Key Laboratory of Advanced Organic Materials, School of Chemistry and Chemical Engineering, Nanjing University, Nanjing 210023, China*
[2] *Shenzhen Research Institute of Nanjing University, Shenzhen 518063, China*
[§] *Junchuan Liang and Yi Hu contributed equally to this work.*

Received: 26 August 2021 / **Revised:** 1 November 2021 / **Accepted:** 3 November 2021

ABSTRACT

Phosphorene, especially black phosphorus (BP), has attracted considerable attention due to the unique characteristics, such as tunable direct bandgap, high carrier mobility, and strong in-plane anisotropy. Recently, a new modification strategy for black phosphorus has been developed by alloying black phosphorus with the congener element arsenic. The elemental composition tuning of black phosphorus with arsenic can not only maintain its special crystal structure and high anisotropy but also modify its electrical and optical properties for the further applications of multifunctional devices. The achieved two-dimensional (2D) black arsenic-phosphorus materials exhibit outstanding optical, electrical, and photoelectric properties, such as very narrow band gap, anisotropic infrared absorption, and bipolar transfer characteristics, presenting great potential in infrared photodetectors and high-performance field effect transistors (FETs). In this review, we introduce the recent progress made in the synthesis and applications of black arsenic-phosphorus, and provide an outlook and perspectives on the current challenges and future opportunities in this field. We hope that this review can bring new insights and inspirations on the further development of 2D black arsenic-phosphorus based materials and devices.

KEYWORDS

black arsenic-phosphorus, two-dimensional (2D) materials, black phosphorus , field effect transistors, mid-infrared photodetectors

1 Introduction

Two-dimensional (2D) materials, a class of layered materials aggregated by van der Waals forces, supply a significant platform for the exploration of fundamental matter properties, promote the generation of novel electronic devices and accelerate the understanding of exotic physical and chemical phenomena [1–19]. The 2D materials depict a fantastic charm due to their exotic electrical, optical, and chemical properties, showing wide applications in the fields of transistors, optoelectronics, sensors, biomedical therapy, energy conversion, etc. [20–37]. Black phosphorus (BP) is a star material in 2D materials that has a tunable band gap, high carrier mobility, and offsets the band gap shortage between graphene and transition metal sulfides [22, 38–43]. Moreover, the outstanding properties of BP enable its great potential in the construction of new generations of photonic and electronic devices.

To extend the applications and enrich the transport behaviors of BP, alloying BP with foreign atoms is an available strategy that can effectively modulate its optical and electrical properties. More recently, black arsenic-phosphorus (b-AsP), which is an alloy of BP obtained by introducing variable percentages of arsenic atoms, has attracted significant attention and interest. B-AsP shares the same crystal structure as BP but has a more variable band gap, which can be simultaneously tuned by the composition and layer thickness [44]. By using molecular beam deposition (MBD) [45], electrochemical delamination exfoliation [46], shear force milling [47], and mechanical exfoliation [48–52], b-AsP with different compositions and features was successfully prepared. To date, the reported applications and properties of b-AsP are diverse, such as Er-doped fiber ultrashort laser generations [46], thermoelectronics [53], photonic microheaters [54], and lithium-ion batteries [47]. In particular, the band gap of b-AsP can be tuned down to ~ 0.15 eV (corresponding to a wavelength of ~ 8.5 μm), indicating that b-AsP is a promising candidate for mid-wave infrared photodetectors [48–52]. Experimentally, Miao et al. reported the mid-infrared photodetection of b-AsP with specific high detectivity beyond 4.9×10^9 Jones in the range of 3 to 5 μm [48]. In addition, as the crystal structure of b-AsP is similar to the crystal structure of BP, b-AsP also shows strong in-plane anisotropic optical absorption and Raman scattering [50, 55, 56]. Moreover, theoretical studies have predicted that b-AsP possesses high electronic mobility and a direct band gap of 1.54 eV, which potentially acts as a highly efficient donor in solar cells [57]. The massive reports and rapid advances of b-AsP reveal its great potential in electronics and photonics and suggest a highly necessary comprehensive review of this fantastic material.

Address correspondence to zhongjin@nju.edu.cn

Hence, to closely track the advances of b-AsP, we perform this review on the recent progress of b-AsP from the aspects of structural features, synthesis, properties, and applications. The structural features of b-AsP are first presented with a comparison to BP. Then, we introduce the preparation of 2D b-AsP using mechanical exfoliation, liquid-phase exfoliation, electrochemical delamination exfoliation, and MBD. Subsequently, the optical and electrical properties of 2D b-AsP, such as the band structure, surface energy, thermoelectric performance, electrically tunable optical properties, Raman scattering effect, and carrier mobility, are discussed. Finally, we list the applications of 2D b-AsP and provide some perspectives on the current challenges and future developments of 2D b-AsP.

2 Crystal structure

Bulk b-AsP crystals have a flake or needle morphology with an obvious layered structure [58]. An individual b-AsP layer is constructed with arsenic and phosphorus atoms with strong in-plane covalent bonds, and each layer is aggregated into a bulk crystal via weak van der Waals interactions (Fig. 1(a)). The weak interlayer force suggests a high possibility of b-AsP crystals being exfoliated into monolayers (Fig. 1(a)). The arsenic and phosphorus atoms are alternatively distributed with the same valence bond form in a single atomic layer b-AsP, forming an orthorhombic lattice with a puckered honeycomb structure (Fig. 1(a)). Owing to the radius of arsenic being larger than that of phosphorus, the lattice constant of b-AsP increases with the increasing proportion of arsenic (Fig. 1(c)). The structural parameters and the band gaps of b-AsP, monoelemental phosphorus and arsenic crystals with bulk and monolayer states are listed in Table 1.

Osters et al. in 2012 combined quantum-chemical calculations and thermodynamic considerations for predicting the stability of the orthorhombic phase from different proportions of phosphorus-arsenic solid solution [58]. Furthermore, they successfully synthesized crystals of o-As_xP_{1-x}, which is the first time that b-AsP was synthesized by chemical vapor transport (CVT). In 2015, Zhu et al. predicted the structural transition in layered As_xP_{1-x} from the α-phase (orthorhombic) to the β-phase (rhombohedral) when x was near 0.83, accompanied by a change from lone-pair electron states in α-P to σ-bond states in β-As [59].

Li et al. in 2020 predicted a dynamically stable Janus single-layer b-AsP by using density functional theory (DFT) calculations. As a result, phosphorus and arsenic atoms are arranged in parallel, forming a puckered honeycomb-like orthogonal phase structure.

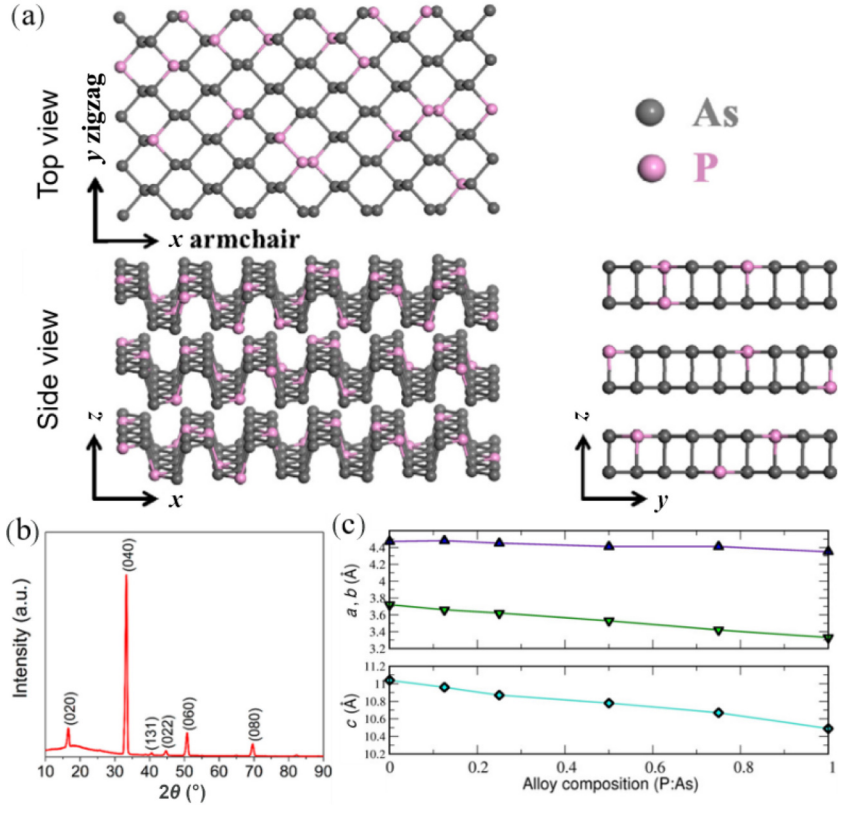

Figure 1 (a) Top view and side view of the b-As_xP_{1-x} crystal. Reproduced with permission from Ref. [46], © Optical Society of America 2019. (b) X-ray diffraction measurement of the b-As_xP_{1-x} crystal. The broad peak at 18° is from Kapton tape, which is used to encapsulate b-$As_{0.83}P_{0.17}$. Reproduced with permission from Ref. [49], © American Chemical Society 2018. (c) Lattice parameter variations of b-AsP crystals as a function of the alloy composition. Reproduced with permission from Ref. [60], © WILEY-VCH Verlag GmbH & Co. KGaA 2020.

Table 1 Comparison of space groups, monolayer thicknesses, interlayer spacings, and energy band gaps between *b*-AsP, monoelemental phosphorus, and arsenic materials

Name	Space group	Thickness (Å)	Interlayer spacing (nm)	E_{gap}^{bulk} (eV)	E_{gap}^{ML} (eV)	References
α-P	*Pmna*	2.11	0.53	0.36	1.60	[61–63]
β-As	$R\bar{3}m$	1.38	0.36	0	1.1–1.3	[64–67]
α-As	*Pmna*	2.39	0.55	0.31	1.52	[44, 64, 68]
α-As_xP_{1-x}	*Pmna*	2.34	0.51	0.15–0.3	0.92–1.54	[48, 50, 57, 69]

This b-AsP was shown to have important consequences for the electronic, optical, and elastic properties [70].

3 Synthesis

3.1 Preparation of bulk *b*-AsP

Early in the 1980s and 1990s, phosphorus arsenic alloys were originally synthesized at robustly high temperature and pressure conditions to study their superconductivity, phase transition, and other physical properties [71–73]. Currently, the CVT method is commonly used to synthesize bulk b-AsP crystals because of the high crystallinity of the product and good repeatability, which is similar to the synthesis of BP [74]. Digital photographs and scanning electron microscopy (SEM) images of bulk b-AsP crystals synthesized by CVT are shown in Figs. 2(a) and 2(b), respectively. Thereafter, a b-AsP single crystal was synthesized for the first time in 2012 by using red phosphorus and gray arsenic as the source materials and PbI_2 as a mineralizer. The three pristine materials were transferred to a silica ampoule and sealed under a high vacuum followed by heating in a furnace with the mixture near the hot end and the empty part near the cold end. After the high-temperature reaction and slow cooling, b-AsP crystals were generated at the cold end. The arsenic composition of b-As_xP_{1-x} obtained by this method can be tuned from 0 to 0.83 [58]. Theoretical calculations and experiments have proven that orthorhombic phase b-As_xP_{1-x} with a puckered honeycomb structure can be realized when $x < 0.83$ [58]. When $x > 0.83$, the stable b-As_xP_{1-x} required the presence of impurities. That is, when $x > 0.83$, pure b-As_xP_{1-x} is difficult to synthesize by the ordinary CVT method.

Subsequently, SnI_4 was used as a mineralizer to replace PbI_2 because it is inexpensive, nontoxic, and easily available. Sn powder was also added to stabilize SnI_4 and prevent the decomposition of SnI_4 at high temperature [50]. A small amount of SnI_4 residual in the as-prepared b-AsP crystals can be removed through refluxing in boiling toluene (ultrasonic bath for 20–45 min). Inductively coupled plasma optical emission spectrometry (ICP-OES) characterization demonstrated that the purity of b-AsP crystals synthesized by this method was above 99.9 at.%. Furthermore, some later studies have further proven that the removal of SnI_4 impurities from the synthesized crystals can also be achieved by soaking in anhydrous acetone or refluxing in boiling toluene [75].

3.2 Preparation of 2D *b*-AsP

3.2.1 *Mechanical exfoliation*

Successful implementation of the mechanical exfoliation method inspired emerging 2D material research. Nanosheets prepared by this method have fewer defects, smooth surfaces, and high carrier mobility. Furthermore, few-layer b-AsP flakes can also be obtained by mechanical exfoliation owing to the weak van der Waals interaction between each pair of b-AsP layers. Due to the advantages of low cost, high efficiency, and convenience, mechanical exfoliation has become the most commonly used method for exfoliating bulk b-AsP crystals [48–51, 54–55]. It is worth noting that the van der Waals interaction between different layered materials plays an important role in the mechanical exfoliation process. For instance, the weak van der Waals interaction resulting from the weak electronegativity between layers leads to a facile formation of few-layer graphene by mechanical exfoliation [3]. Transition metal dichalcogenides (TMDCs) have intrinsically passivated surfaces without dangling bonds, resulting in weak van der Waals interactions. Thus, large quantities of few-layer TMDCs flakes can easily be obtained by facile mechanical exfoliation [76]. Nevertheless, because of the multiple and inhomogeneous compositions with a high electronegativity of b-AsP, which result in a much stronger interaction among layers than other materials, it is more difficult to obtain few-layer b-AsP flakes by mechanical exfoliation. The yields of b-AsP nanosheets obtained by mechanical exfoliation are usually low, and the surface of the b-AsP nanosheets generally has adhesion residues, leading to open challenges to 2D material development.

3.2.2 *Liquid-phase exfoliation*

Considering the low yield of mechanical exfoliation, liquid-phase exfoliation conducted by dispersing the layered materials in a liquid phase under ultrasonication to obtain a large number of nanosheets [77]. The mechanism of liquid-phase exfoliation

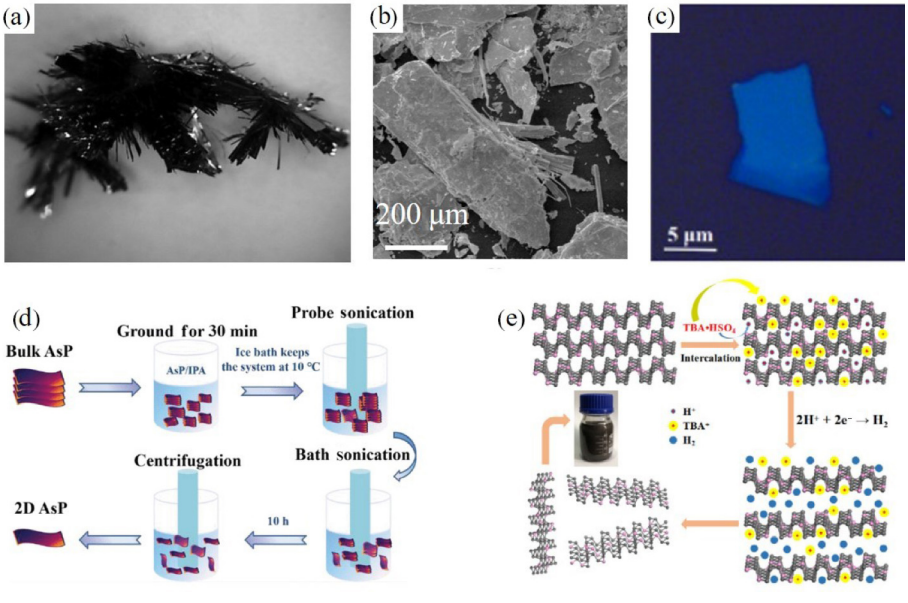

Figure 2 (a) B-$As_{0.83}P_{0.17}$ crystal synthesized by CVT. Reproduced with permission from Ref. [58], © WILEY-VCH Verlag GmbH & Co. KGaA 2012. (b) SEM image of b-$As_{0.2}P_{0.8}$. Reproduced with permission from Ref. [53], © American Chemical Society 2020. (c) Optical image of mechanically exfoliated few-layer b-$As_{0.83}P_{0.17}$. (d) Schematic illustration of the preparation of 2D b-AsP nanosheets by the liquid-phase exfoliation method. Reproduced with permission from Ref. [78], © IEEE 2020. (e) Schematic illustration of the liquid-phase electrochemical exfoliation procedure. Reproduced with permission from Ref. [46], © Optical Society of America 2019.

includes ion intercalation/exchange and ultrasonic-assisted exfoliation. In this process, huge energy generated by the formation and collapse of cavitation bubbles, leading to the separation of layered materials [77]. Liquid-phase exfoliation was used mainly for the preparation of graphene at first and then expanded to other 2D materials [79–81].

Figure 2(d) illustrates a typical scheme of the liquid-phase exfoliation of b-AsP. The commonly used solvent is relatively polar isopropanol (IPA), whose surface energy is equivalent to the surface energy of nanosheets. When bulk b-AsP is exfoliated into nanosheets by ultrasonication, the b-AsP nanoflakes are well dispersed in the isopropanol solvent and simultaneously stabilized against reaggregation. With the generation of a large amount of heat, which would lead to an elevated temperature, the ultrasound process must be performed in an ice bath to prevent the oxidation of *b*-AsP nanoflakes [52, 78].

Compared to the b-AsP nanosheets synthesized by mechanical exfoliation, the yield of nanoflakes achieved by the liquid-phase exfoliation method is significantly enhanced. An easier synthesis method is conducive to the further development of studies and application of b-AsP. However, many shortcomings of b -AsP prepared by liquid-phase exfoliation still need to be solved. For example, the lateral size of nanosheets is insufficient, and violent ultrasonic peeling causes many defects on the surface of nanosheets, restricting their application in nanoelectronics. In addition, many single crystals deteriorate and are wasted after liquid-phase exfoliation, suggesting the necessity of further improvement of methods and the application of products.

3.2.3 *Electrochemical exfoliation*

Electrochemical exfoliation based on the redox process is a relatively efficient method for the generation of 2D materials. Ions in the electrolyte migrate from the electrolyte to the interspace of the layered bulk under an electric field, which can easily break the weak van der Waals force among layers. With the ions inserted into the electrode, the interlayer spacing of the layered bulk expands, leading to peeling off the nanosheets from the electrode bulk materials. However, under high potential, such a method inevitably causes the oxidation of bulk materials when used as an anode. In contrast, the oxidation issue can be efficiently addressed when the layered bulk material serves as a cathode, in which cations are inserted into the interlayer, resulting in expansion.

Shi et al. imitated the previous method used for exfoliating BP and successfully exfoliated b-$As_{0.83}P_{0.17}$ nanosheets [82–85]. In this report, tetrabutylamine hydrogen sulfate (TBA·HSO_4) was used as the electrolyte, and b-AsP was used as the cathode. The reaction diagram of the exfoliation process is shown in Fig. 2(e). Initially, only flattened TBA^+ can migrate to the interlayer gap. Subsequently, hydrogen ions ionized by HSO_4^- can also be inserted between the layers to undergo a reduction reaction and generate hydrogen, which will accumulate exfoliation by forming small bubbles. As TBA^+ spreads out in the interspace, the weak van der Waals interaction can be destroyed, resulting in successful peeling off of b-$As_{0.83}P_{0.17}$ nanosheets [46].

Electrochemical exfoliation is a common method to synthesize 2D materials because of its advantages of being highly efficient and environmentally friendly. However, a severe exfoliating environment will also generate enormous defects on the surface of 2D materials. Therefore, further study is needed to prepare single-layer b-AsP nanosheets with excellent quality and performance.

3.2.4 *Molecular beam deposition of b-AsP thin film*

In 2018, a 3-inch b-$As_{0.78}P_{0.22}$ film was successfully deposited on a large-area InP wafer by MBD [45], in which three effusion cells generate phosphorus and arsenic atomic beams under ultrahigh vacuum (Fig. 3(a)). A stepping motor drives the substrate on the sample stage to controllably rotate and tilt for uniform deposition. Reflection high-energy electron diffraction (RHEED) is employed to monitor the growth of phosphorus-arsenic crystal films. MBD has very high requirements on the vacuum of the chamber and the temperature of the substrate for strict control over the quality of the crystal film. The temperature of the substrate greatly affects the speed of deposition on the substrate, which in turn affects the quality of the crystal film. After subsequent annealing, the crystallinity of the film can be highly improved. Transmission electron microscopy (TEM) was employed to illustrate the lattice structure of the formed b-AsP film (Fig. 3(b)). As shown in Fig. 3(c), the 6 nm thick b-AsP film obtained with a highly preferred orientation could be encapsulated with a layer of Al_2O_3 film formed through low-temperature atomic layer deposition (ALD) to prevent the b-AsP film from oxidation. The corresponding Raman spectra of the film is also identical to the Raman spectra previously reported (Fig. 3(d)). High-quality b-AsP films with controllable thickness and adjustable composition can be obtained, promoting the study of the integration of b-AsP into various electronic and optoelectronic devices.

Previous works reported the bottom-up synthesis of bulk b-AsP with varied As/P atomic ratios through the CVT method.

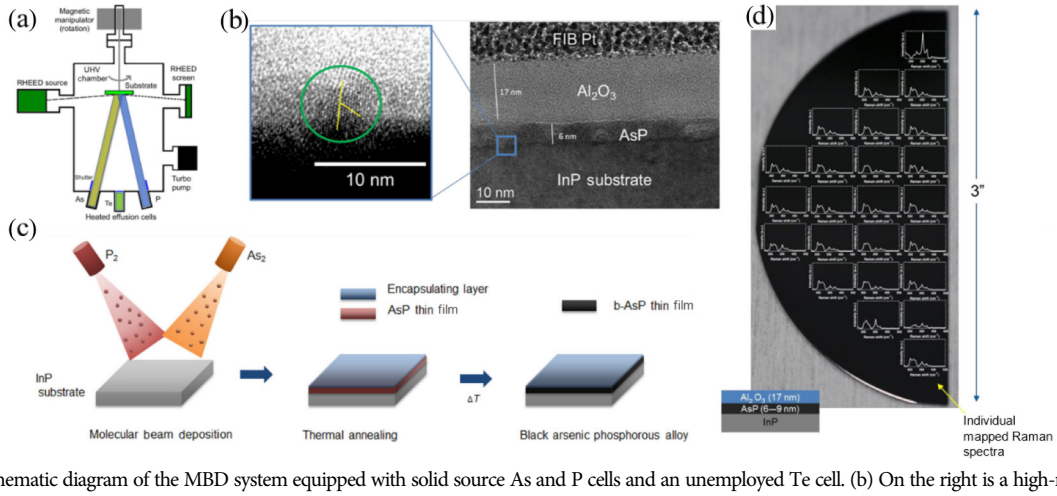

Figure 3 (a) Schematic diagram of the MBD system equipped with solid source As and P cells and an unemployed Te cell. (b) On the right is a high-resolution TEM (HRTEM) image of the sample cross section. On the left is a magnified image of the cross section, where the yellow lines represent directions normal to planes (131) and (002). (c) Schematic illustration of the synthesis of b-AsP alloys. (d) The mapped Raman spectra of a half-wafer. The inset shows the sample section diagram. Reproduced with permission from Ref. [45] © American Chemical Society 2018.

Moreover, top-down methods were also used to exfoliate few-layer b-AsP materials. However, it is still difficult to obtain single-layer b-AsP materials with good crystal quality, owing to the uneven distribution of phosphorus atoms and arsenic atoms, which causes the increase of interlayer non-dispersive interactions. So far, there is only one report on the bottom-up synthesis of few-layer b-AsP films by the MBD method [45], and the bottom-up synthesis of monolayer b-AsP has not been realized. The thickness and quality of b-AsP still need to be further controlled. Although the conventional chemical vapor deposition (CVD) method is mature, there is still no successful instance of growing b-AsP by the CVD method. Therefore, it is an urgent problem to precisely control the thickness of b-AsP, especially the growth of monolayer b-AsP. It is very likely that more exciting properties of b-AsP could be revealed and more applications could be realized after achieving the control synthesis of monolayer b-AsP, as predicted by theoretical calculations.

4 Properties

4.1 Band structure

B-AsP is a semiconductor with a direct bandgap similar to BP. The bandgap of BP previously reported is 0.3–2.2 eV [38–40]. As the number of layers decreases, the gap gradually increases until reaching 2.2 eV in a single layer. However, the bandgap of bulk b-AsP is less than 0.3 eV and decreases with increasing arsenic concentration. The b-$As_{0.83}P_{0.17}$ synthesized with the highest arsenic concentration has a bandgap of 0.15 eV measured with infrared absorption. B-AsP with a bandgap of 0.15–0.3 eV can absorb light with a wavelength of 4.13–8.27 μm, which can be well utilized for technologically important slack in the long wavelength infrared (LWIR) regime and expand its application to optoelectronics [69, 86].

As shown in Fig. 4(a), Liu et al. systematically conducted infrared absorption measurements of b-AsP with different arsenic concentrations and confirmed the relationship between the bandgap and the arsenic concentration. When the arsenic concentration changes from 0 at.% to 40 at.%, the bandgap is drastically reduced from 0.3 to approximately 0.17 eV. As the arsenic concentration increases further, the bandgap changes are no longer as pronounced as before, only from approximately 0.17 to approximately 0.16 eV [50].

In 2016, Xie et al. combined the Perdew–Wang 1991 (PW91) functional with the Heyd–Scuseria–Ernzerhof hybrid functional (HSE06) to calculate single-layer phosphorus-arsenic alloys with α, β, γ, δ, and ε phases (Figs. 4(b) and 4(c)). The direct band gap of α-phase single-layer b-AsP calculated by PW91 is 0.90 eV, while that calculated by HSE06 is 1.54 eV. The band gap calculated with PW91 is often lower than the bandgap calculated with HSE06, but the band type at the Fermi level calculated by the two methods is basically the same with only minor differences. In this report, the structure of α-AsP is an ideal structure, in which arsenic and phosphorus atoms are alternately arranged to form a puckered orthogonal hexagonal structure. However, the atoms of the two different elements are arranged randomly in actual b-AsP crystals, rather than as uniform as reported in the article [57].

By using DFT calculations, Sun et al. also found that the band gap of b-AsP is sensitive to uniaxial strain, which is applied to the armchair and zigzag directions (Figs. 4(d) and 4(f)). Particularly, owing to the transition from a direct bandgap to an indirect bandgap, the bandgap will accordingly increase and then slightly decrease after reaching the maximum value when a tensile strain is applied in the armchair direction [87].

In view of the features of heavy elements for both P and As, the influence of the spin-orbit coupling (SOC) effect on the band gaps of b-AsP was also studied. In 2018, Yu et al. proved the dependence of the bandgap of thin-layer b-AsP on the SOC through Fourier transform infrared (FTIR) spectroscopy and DFT calculations. As shown in Fig. 4(e), the valence band maximum (VBM) and conduction band minimum (CBM) of b-AsP will split into one newly generated subband, forming four infrared energy gaps [55].

4.2 Surface energy

When the thickness of b-AsP is thinned to the atomic level, the material has a tremendous specific surface area, leading to a great desire of researchers to study its surface energy to promote the understanding of the surface structure, reconstruction and roughening [88–90]. In 2020, Bousa et al. measured the surface energy of b-AsP alloys with two different compositions (b-As_1P_3 and b-As_2P_3) through inverse gas chromatography equipped with

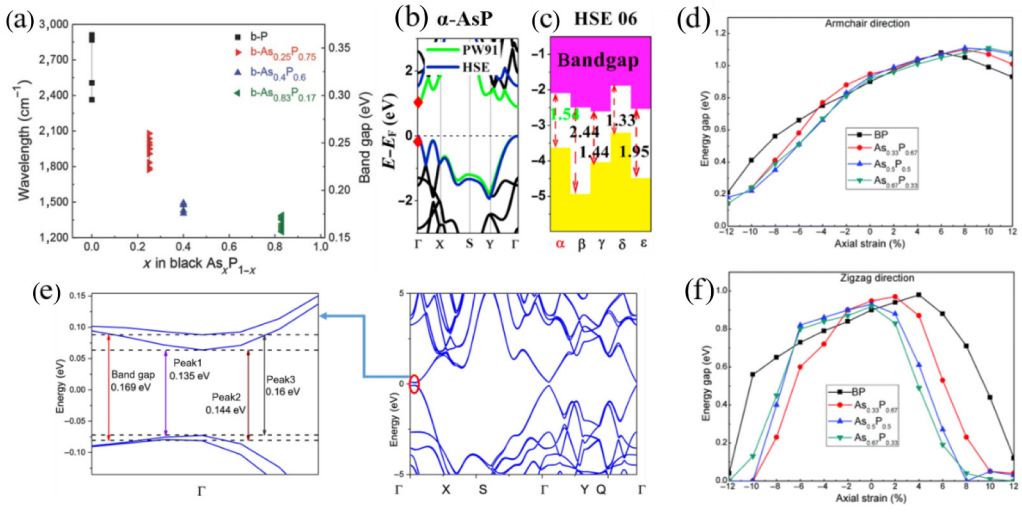

Figure 4 (a) Summary of the *x*-dependent infrared absorption wavelength and band gaps of b-As_xP_{1-x}. Reproduced with permission from Ref. [50], © WILEY-VCH Verlag GmbH & Co. KGaA 2015. (b) Electronic band structure of the monolayer α-AsP calculated by PW91 and HSE06. (c) The energy band gaps of binary phosphorus-arsenic alloys with different crystal structures calculated by the HSE06 method. Reproduced with permission from Ref. [57], © Elsevier Ltd. 2016. (d) and (f) Strain dependence of the energy band gap along the armchair and zigzag directions. Reproduced with permission from Ref. [87], © the Owner Societies 2016. (e) On the right is a schematic diagram of the band structure of multilayer b-AsP considering SOC. On the left is an enlarged image of the energy band, in which the band has been split into four sub-bands. Reproduced with permission from Ref. [55], © IOP Publishing Ltd 2018.

a surface energy analysis instrument (IGC-SEA) [60]. As seen from the DFT calculation results in Fig. 5(a), the surface energy of the material basically does not change greatly with the variation of the element ratio in b-AsP. Figure 5(b) illustrates the total surface energy of the material by considering dispersion and nondispersive components. The difference in total surface energy among b-As_1P_3, b-As_2P_3, and BP is not obvious after considering the error bars, which implies that the addition of arsenic atoms has almost no effect on the surface energy of b-AsP. Moreover, Fig. 5(b) also shows that the surface energy of the b-As_1P_3 and *b*-As_2P_3 alloys varies little with respect to the surface coverage of the probe molecules. The relationship between the surface energy and the surface coverage of the probe molecule is thus shown in Fig. 5(c). As the surface coverage increases, the measured surface energy decreases drastically at first and then decreases slowly. At a low surface coverage, the probe would first adsorb on sites with higher surface energy, such as steps, edges, and cavities. Therefore, the measured surface energy can be used to evaluate the flatness of the material surface [91]. The almost constant surface energy with increasing coverage demonstrates that the flat surface of b-AsP basically does not have these high-energy sites, and it is basically a flat surface (Fig. 5(b)). The relationship between the acid-base component and the coverage of the probe molecule shown in the inset of Fig. 5(b) reveals that the acid-base component of b-As_2P_3 and BP contributed just approximately 3%, indicating that the surface energy is contributed mainly by the dispersion factor. Herein, the limited acid-base component (13 mJ/m^2) of b-As_1P_3 might be ascribed to surface oxidation.

4.3 Thermoelectricity

Thermoelectric materials can reversibly convert the electrical and thermal energy within the materials, realizing the energy conversion and utilization of waste energy. Three factors, including the Seebeck effect, Peltier effect, and Thomson effect, are usually considered to evaluate the performance of thermoelectric materials. The thermoelectric efficiency of the material can be evaluated by the thermoelectric figure of merit (ZT). ZT can be calculated by the formula $ZT = S^2\sigma T/k$, where S is the Seebeck coefficient, also known as thermoelectric power (TEP), σ is the electrical conductivity, T is the absolute temperature, and k is the thermal conductivity. Thus, the thermoelectric performance of a material is determined by the Seebeck coefficient and electrical and thermal conductivity. In addition, for a thermoelectric device, it's favorable to have both high electrical conductivity and low thermal conductivity in the direction between the cold end and the hot end [92–94]. Similar to BP, b-AsP also has anisotropic thermal conductivity and electrical conductivity, enabling b-AsP to be a potential candidate for thermoelectrical applications.

In 2020, Karki et al. measured the thermoelectric power and electrical conductivity of b-AsP by fabricating a thermoelectric device (Fig. 6(a)). Figure 6(b) shows the temperature dependence of the TEP of b-As_xP_{1-x} with different values of x. The Seebeck coefficient changed with temperature almost in accordance with $S \sim aT^{1/3}$ when x = 0, 0.2, and 0.5, and the TEP value of b-$As_{0.2}P_{0.8}$ reached 800 μV/K even at room temperature, indicating a potential 2D variable range hopping (VRH) model within materials [95]. However, pure arsenic and b-$As_{0.83}P_{0.17}$ showed a very small TEP with a value of 7 μV/K at room temperature. Figure 6(c) shows the relationship between the resistance of b-As_xP_{1-x} and the temperature. B-As_1P_0 and b-$As_{0.83}P_{0.17}$ basically

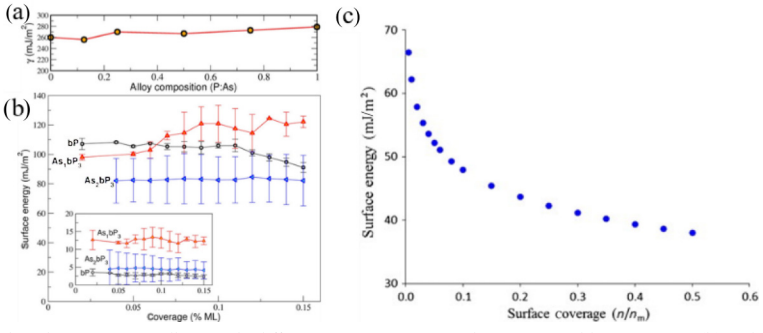

Figure 5 (a) Surface energies of phosphorus-arsenic alloys with different compositions in their most stable structures. (b) Relationship between the total surface energy and surface coverage of BP (black circles), b-As_1P_3 (red triangles), and b-As_2P_3 (blue triangles) alloys. The inset shows the relationship between the acid-base components of the total surface energy and surface coverage. Reproduced with permission from Ref. [61], © WILEY-VCH Verlag GmbH & Co. KGaA 2020. (c) Dispersive surface energy profile when the surface coverages are between 0.5% and 50%. Reproduced with permission from Ref. [91], © Elsevier B.V. 2014.

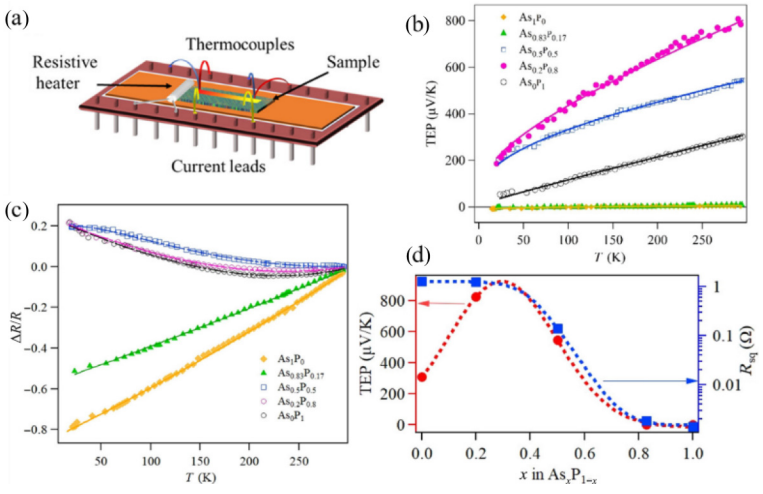

Figure 6 (a) Schematic diagram of the thermoelectric test system. (b) Relationship of different compositions of b-AsP between TEP and temperature. (c) The normalized resistance $\Delta R/R = (R(T) - R(RT))/(R(RT))$ variation as a function of the temperature. (d) The fitting curve of TEP (left axis) and 4-probe resistance (right axis) with the arsenic concentration. Reproduced with permission from Ref. [53], © American Chemical Society 2020.

exhibited the resistance characteristics of the metal, in which the resistance simply increased with increasing temperature. However, when x = 0, 0.2, and 0.5, the resistance of b-As_xP_{1-x} is negatively related to temperature at low temperature but positively at high temperature, which conforms to the relationship of $\Delta R/R = aT + bexp(T^{\wedge}(-1/3))$, further conforming to the 2D VRH mechanism in the transmission process. By fitting the TEP and resistance values of several alloys (Fig. 6(d)), both TEP and resistance values can be predicted to reach their maximum values of 1,000 μV/K and 1 Ω when x is approximately 0.2. When x < 0.2, the TEP of the material decreases significantly with decreasing arsenic concentration, but the conductivity will not be improved; when x > 0.2, the TEP of the material decreases as the arsenic concentration increases, but x > 0.2 significantly improves the electrical conductivity of the material [53]. Table 2 shows the electron transmission characteristics (Seebeck coefficient, conductivity, and PF) of thermoelectric materials at room temperature, demonstrating the excellent thermoelectric performance of phosphorus-arsenic alloys.

4.4 Optical properties

4.4.1 Infrared absorption effect

The unique puckered orthogonal hexagonal structure of b-AsP and the highly tunable compositions enable diverse optical properties. The direct bandgap of 0.15–0.3 eV corresponds to a mid-infrared wavelength range of 4.13 to 8.27 μm. The high tunability of the composition enabled the material to have a versatile infrared absorption effect. Figure 7(a) exhibits the infrared absorption curve of b-As_xP_{1-x} with different concentrations of arsenic, in which the absorption edge of the infrared absorption redshifts with increasing arsenic. As shown in Fig. 7(b), the band gap of b-AsP gradually narrows down with the incorporation of arsenic atoms, resulting in a gradual decrease in its infrared absorption wavenumber [50]. In addition, the polarization-resolved infrared absorption spectrum of b-AsP in Fig. 7(c) demonstrates that b-AsP also has anisotropic absorption behavior similar to BP. The maximum absorption arises at an angle of 135°, corresponding to the x-axis of b-$As_{0.83}P_{0.17}$, while the minimum absorption arises at an angle of 45°, corresponding to the y-axis of b-$As_{0.83}P_{0.17}$. In 2018, Yu et al. demonstrated that b-AsP has three weaker absorption peaks in a longer wavelength range, as depicted in Fig. 7(d). Owing to the SOC effect, the original VBM and CBM split a sub-gap, resulting in the generation of three additional infrared absorption peaks. In addition, the three subpeaks also have anisotropic absorption behavior, which was consistent with the same anisotropic law for band-edge absorption. Furthermore, the subpeaks corresponding to infrared absorption are electrically tunable. The gate voltage applied to the materials enlarged the absorption, which is revealed at the subpeak, valley and absorption edge. This change in absorption was attributed to the change in the free carrier concentration induced by the gate voltage, which in turn affects

Table 2 Room-temperature electronic transport properties (S, ρ, and PF) of some thermoelectric materials at 300 K

Compound	TEP(S) (μV/K)	P (Ω·m)	PF = S^2/ρ (μW/(m·K^2))	References
BP	313.0	4.66×10^{-3}	22.38	[53]
b-$As_{0.2}P_{0.8}$	803.0	5.85×10^{-3}	110.26	[53]
b-$As_{0.5}P_{0.5}$	550.9	9.59×10^{-4}	316.54	[53]
b-$As_{0.83}P_{0.7}$	7.4	8.34×10^{-6}	6.57	[53]
Bi_2Se_3	−105	1.92×10^{-5}	575.0	[96]
Sb_2Te_3	129	4.76×10^{-5}	349	[97]
PbTe	451	4.34×10^{-4}	468	[98]
$SnSe_{1.98}Br_{0.02}$	−201	2.70×10^{-4}	149	[99]
ZnO	−175	2.00×10^{-4}	153	[100]

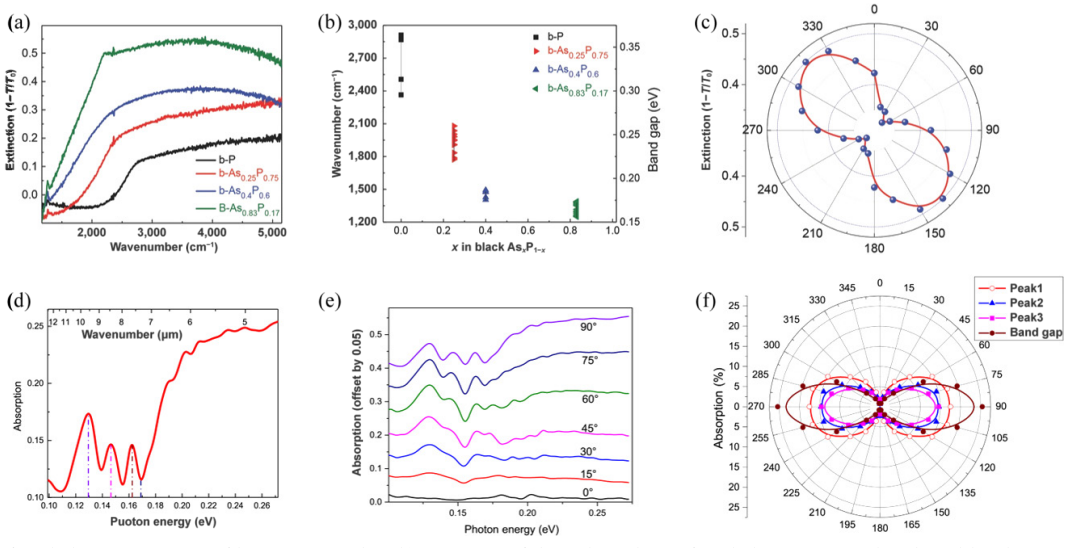

Figure 7 (a) Infrared absorption curves of b-As_xP_{1-x} samples. (b) Summary of the x-dependent infrared absorption wavelength and band gaps of b-As_xP_{1-x}. (c) Polarization of the extinction intensity at 2,200 cm^{-1}. Reproduced with permission from Ref. [50], © WILEY-VCH Verlag GmbH & Co. KGaA 2015. (d) The absorption spectrum measured by FTIR reflection spectroscopy (the dashed lines indicate the three subgap peaks). Vg = 0 V; T = 300 K; P = 1 bar. (e) Fourier transform infrared (FTIR) spectra of the sample with different rotation angles of the polarizer. (f) Polarization of the infrared adsorption corresponding to the band gap and three subpeaks in (d). Reproduced with permission from Ref. [55], © IOP Publishing Ltd. 2018.

the infrared absorption intensity [55].

4.4.2 *Raman scattering effect*

Compared with BP and gray arsenic, the b-AsP alloy has multiple element types, resulting in a multiple bond form and showing several groups in Raman peaks. The Raman peaks of b-AsP were distributed in three main regions (Fig. 8(a)). The low-frequency region below 275 cm^{-1} contains vibration information for the As–As bond, while the high-frequency region above 350 cm^{-1} contains vibration information for the P–P bond. The Raman peaks in the region between 275 and 350 cm^{-1} could thus reflect the vibration of the P–As bond. After increasing the arsenic concentration, the relative intensity of the Raman peaks in the low-frequency region became intense, whereas the opposite phenomenon was observed for the high-frequency region. When 50% of the phosphorus atoms were replaced with arsenic atoms, the most intense Raman peaks in the middle frequency region were exhibited. Furthermore, the redshift of Raman for phosphorus was also raised after increasing the concentration of arsenic, as shown in Fig. 8(b), which can be attributed to the length of the P–P bond being shorter than the length of the As–As bond. When a small number of arsenic atoms were incorporated into the BP lattice, the arsenic atoms will be compressed, resulting in a shorter bond length due to the influence of surrounding P atoms. However, this effect weakens when the concentration of arsenic atoms increases, as shown by the redshift of Raman peaks, resulting in an enlarged As–As bond length. In contrast, when the concentration of arsenic atoms increases, arsenic in the crystal lattice will occupy most of the positions for phosphorus, and a small part of the P–P bonds will be affected by the surrounding arsenic atoms, thus enlarging the bond length of the P–P bond and redshifting the Raman peak [53]. Because b-AsP is a layered material, the Raman shift displays no change with the stacking number of layers, but the intensity changes (Fig. 8(d)) [50]. The Raman feature of the b-AsP alloys is also anisotropic due to the unique crystal structure characteristics of BP. Previous studies have shown that the Raman scattering of BP shows a polarization behavior related to the crystal orientation [101, 102]. In 2015, Liu et al. observed such polarization behavior in the low-frequency region, the Raman peaks of different vibration modes of arsenic in b-AsP alloys also have polarization behavior, as shown in Figs. 8(e) and 8(f) [50].

4.5 Carrier mobility

Mobility is an important parameter that characterizes the conductivity of semiconductors and affects the operating speed of the device. As early as 1987, Shirotani et al. started to focus on the superconductivity of phosphorus-arsenic alloys. Phosphorus-arsenic alloys have been found to be able to achieve complete conductivity with a resistance of 0 under high pressure, and the superconducting temperature showed high pressure dependence (Fig. 9(a)) [71]. Recently, the conductivity of monolayer b-AsP has been more extensively studied with emerging studies on 2D materials. In 2015, Shojaei et al. simulated the carrier drift behavior of b-AsP under different original topological arrang ements, demonstrating good performance as BP. Specifically, the electron mobility of the dynamically stable orthogonal phase of b-AsP in the zigzag direction has been demonstrated to be as high as 10,460–25,840 $cm^2/(V·s)$. In contrast, the high mobility of holes is poor in the armchair direction, which in turn provided anisotropy for carrier transport [103]. In 2016, Xie et al. stimulated exciton solar cells using a b-AsP monolayer as a donor, achieving high electron mobility of 14,000 $cm^2/(V·s)$ [57]. Experimental efforts on b-AsP have demonstrated good bipolar transport characteristics and high hole mobility of approximately 307 $cm^2/(V·s)$ by building field effect transistors (FETs), implying the tremendous application potential of b-AsP.

5 Applications

5.1 Field effect transistors

The FETs could tune the conductivity of the material between the source and drain by applying a voltage on the gate. In 2015, Liu et al. exfoliated b-$As_{0.2}P_{0.8}$ nanosheets onto an oxidized and polished silicon wafer to fabricate a classic FET device (Fig. 9(b)). The thick nanosheet showed no change in I_{ds} during the gate voltage sweep from −45 to 45 V, as shown in Fig. 9(d). However, the b-AsP

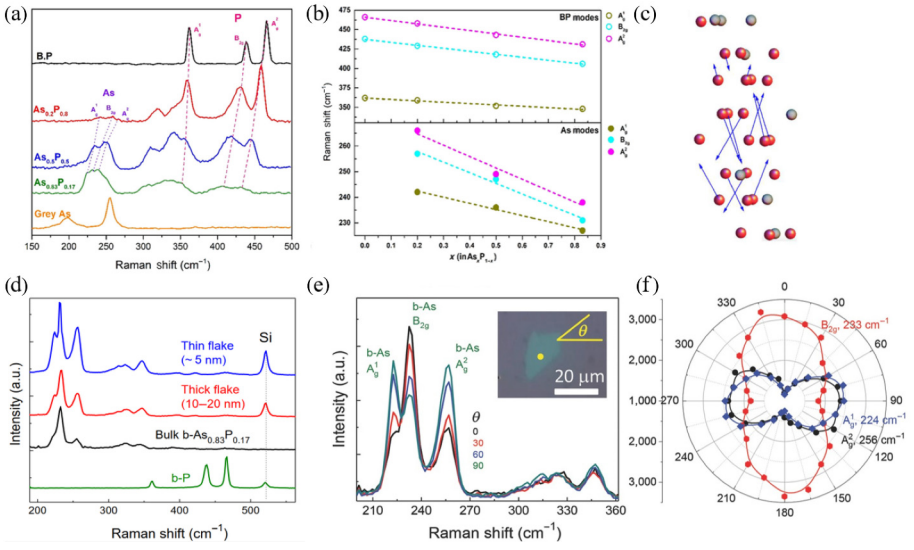

Figure 8 (a) Raman spectra of BP, gray As, and b-As_xP_{1-x} with different chemical compositions. (b) Relationship between Raman shift and arsenic concentration (x) for P–P (top) and As–As (bottom) vibrational modes. Reproduced with permission from Ref. [53], © American Chemical Society 2020. (c) Schematic of an As–As vibrational mode at 208 cm^{-1} of bulk b-$As_{0.75}P_{0.25}$. As atoms are in red and P atoms are in gray. Reproduced with permission from Ref. [45], © American Chemical Society 2018. (d) Raman spectra of bulk (black), thick flakes (red), and thin flakes (blue) of b-$As_{0.83}P_{0.17}$. (e) Local Raman spectra of b-$As_{0.83}P_{0.17}$ at different polarization angles, which reflect mainly the polarization characteristics of b-As. The inset shows the optical image of the sample and indicates the polarization angle. (f) Polarization of the intensity of Raman peaks at 256, 233, and 224 cm^{-1}, which correspond to the A_g^1, B_{2g}, and A_g^1 modes of b-$As_{0.83}P_{0.17}$. Reproduced with permission from Ref. [50], © WILEY-VCH Verlag GmbH & Co. KGaA 2015.

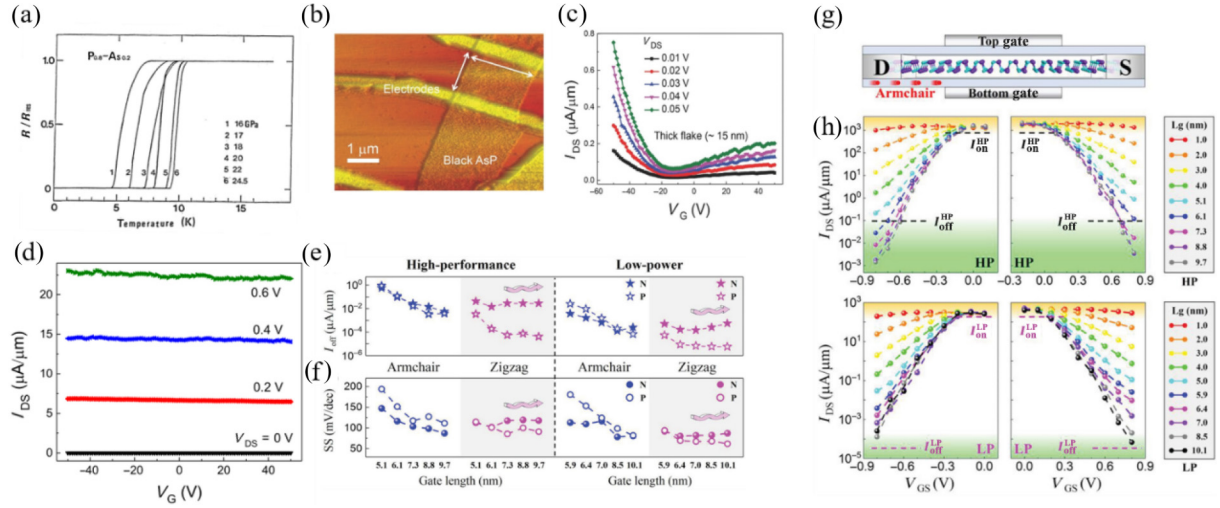

Figure 9 (a) The relationship between the electrical conductivity and temperature of b-$As_{0.2}P_{0.8}$ under different pressures. Reproduced with permission from Ref. [71], © IOP Publishing 1987. (b) Atomic force microscope (AFM) image of the b-AsP FET. (c) Transfer curves of a 15 nm thick b-$As_{0.83}P_{0.17}$ flake. (d) I_{DS}–V_G characteristics of a thick b-$As_{0.83}P_{0.17}$ flake. The thickness of the flake is approximately 60 nm based on AFM measurements. Reproduced with permission from Ref. [50], © WILEY-VCH Verlag GmbH & Co. KGaA 2015. (e) The relationship between the off-state current and the gate length for HP and LP devices along the zigzag and armchair directions. (f) Subthreshold swing as a function of the gate length for HP and LP devices along the armchair and zigzag directions, respectively. (g) Schematic diagram of a monolayer b-AsP FET along the armchair direction. (h) Transfer characteristics of n-type and p-type b-AsP FETs with different gate lengths along the armchair direction for HP and LP devices, respectively. Reproduced with permission from Ref. [56], © Wiley-VCH Verlag GmbH & Co. KGaA 2020.

nanosheet with a thickness of 15 nm showed typical bipolar transfer characteristics and high hole mobility of 110 $cm^2/(V·s)$ (Fig. 9(c)) [50]. Then, Long et al. reported a FET of b-AsP that had high hole mobility of 307 $cm^2/(V·s)$ at a drain voltage of 0.01 V [48]. To study the ballistic transport characteristics of 2D b-AsP, Zhou's group utilized the FET model to simulate and calculate the transport performance of 2D b-AsP (Fig. 9(g)), demonstrating that the b-AsP FET conformed to the International Technology Roadmap for Semiconductors (ITRS) requirements and was more suitable for high-performance (HP) applications than for low-power consumption (LP) applications (Fig. 9(h)). In addition, the ballistic transportation of b-AsP FET devices also displayed anisotropic behavior (Figs. 8(e) and 8(f)) [56]. There are distinct differences between n-type and p-type FETs in varied directions of the b-AsP. As the p-type semiconductor changed more intensely in the zigzag direction, the I_{off} in the armchair direction would be generally higher than the I_{off} in the zigzag direction when the gate length increased. In addition, the variation in subthreshold swing (SS) in different directions also showed the anisotropic behavior of the b-AsP FETs. This work also revealed that the smaller energy-delay product (EDP) of 4.05×10^{-30} and -1.35×10^{-29} (J·s)/μm suggested the great application potential of b-AsP in FETs [56].

5.2 Mid-wave infrared photodetectors

The band gap of b-AsP falls from 0.15–0.3 eV, which indicates good absorption at mid-infrared wavelengths of less than 8 μm. The first mid-infrared photodetector based on b-AsP showed a relatively high specific detectivity (D^*) of 2.4×10^{10} cm·$Hz^{1/2}$/W (Fig. 10(a)) [51]. Subsequently, the infrared detector made of *b*-AsP depicted a responsivity of 15–30 mA/W corresponding to wavelengths ranging from 2 to 8 μm and a rise time of 0.54 ms (Figs. 10(b) and 10(c)). Current noise caused by disorders and defects in 2D b-AsP is a key obstacle in improving the detectivity of equipment. In 2017, Long et al. reported a mid-infrared detector with a relativity low current noise through an innovative heterostructure design (Fig. 8(d)). The b-AsP nanosheet was superimposed on a MoS_2 nanosheet to form a P–N heterostructure that suppressed the current noise by generating an energy barrier. The noise equivalent power (NEP) is one order of magnitude lower than the NEP of the ordinary b-AsP detector reported previously; D^* is nearly two orders of magnitude higher than the D^* of commercialized infrared detectors (Figs. 10(e) and 10(f)) [48]. Degradation of b-AsP would greatly reduce the performance of the detector and thus limit its infrared application. Yuan et al. reported a sandwich-structure hBN/b-$As_{0.83}P_{0.17}$/hBN structure to make a stable mid-infrared detector (Figs. 10(g) and 10(h)), demonstrating an outstanding responsivity for several months of 90 mA/W in an ambient environment [49].

5.3 Er-doped fiber ultrashort lasers

With the development of long-distance data transmission [104], biomedical imaging [105], laser engraving [106], and welding technologies [107], ordinary lasers are unable to meet technical requirements. The emergence of technologies such as high-brightness laser diode pump light sources and Er-doped fiber (EDF) amplifiers in the 1980s promoted the development of short-pulse, high-energy, and long-lasting fiber lasers [108, 109]. Recently, a fiber laser with excellent performance was equipped with a saturable absorber (SA), which is a basic portion of a laser system that modulates cavity loss and realizes ultrashort pulses. 2D materials are promising candidates for saturated absorbers due to their thickness-dependent band gap and large specific surface areas. Many suitable 2D materials, such as graphene, TMDCs, Bi_2Te_3, $SnSe_2$, and b-P, have been utilized to fabricate the SA of lasers to achieve ultrashort pulse modulation [110–114]. B-AsP features a highly adjustable band gap and excellent optical properties, making it a powerful candidate for SA applications. In 2019, Shi et al. reported for the first time that a b-AsP alloy was used as an SA to fabricate an Er-doped fiber laser (Fig. 11(a)). As a result, the laser operated at a maximum output power of 3.68 mW when the pump power was 40 mW (Fig. 11(b)). The pulse duration lasted for 9.18 μs, with a frequency of 38.47 kHz (Fig. 11(c)) [46]. Shu et al. reported that an Er-doped laser using b-AsP as the SA showed a pulse duration of only 828 fs, but a frequency of 8.49 MHz, with a signal-to-noise ratio of 61 dB, and the output laser spectrum was stable for 7 h (Figs. 11(d)–11(f)). Comparable performance was also shown in Th-doped lasers with a high signal-to-noise ratio of 68.8 dB, reflecting the huge application potential of b-AsP as a saturated adsorber [52].

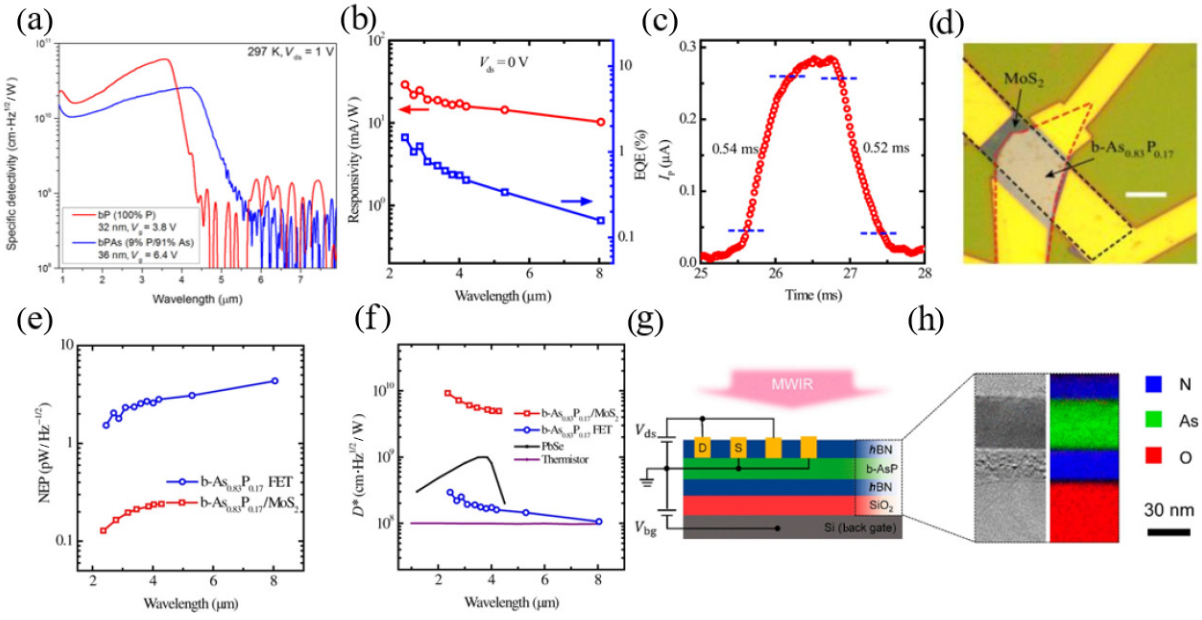

Figure 10 (a) The relationship of specific detectivity with the wavelength of the BP and b-AsP photodetectors. Reproduced with permission from Ref. [51], © American Chemical Society 2017. (b) Relationships of photoresponsivity R (left) and external quantum efficiency (EQE) (right) with wavelengths ranging from 2.4 to 8.05 mm. (c) Photoresponse of a typical device excited by a 4.034 μm laser (21.5 W/cm^2) at V_{ds} = 0 V and V_g = 0 V. (d) Optical image of the b-As$_{0.83}$P$_{0.17}$/MoS$_2$ heterostructure device. The scale bar is 5 μm. (e) The relationship of the NEP with the wavelength of a b-AsP FET device (blue open circles) and a b-AsP/MoS$_2$ heterostructure (red open squares). (f) The relationship of the specific detectivity (D^*) with the wavelength. The purple and dark lines are commercial specific detectivity for a thermistor bolometer and PbSe MIR detectors at room temperature, respectively. Reproduced with permission from Ref. [48], © The authors 2017. (g) Cross-sectional cartoon image of the hBN/b-As$_{0.83}$P$_{0.17}$/hBN heterostructure photodetector. (h) The cross section of the device by TEM is shown on the left. The elemental analysis mapping is shown on the right. Reproduced with permission from Ref. [49], © American Chemical Society 2018.

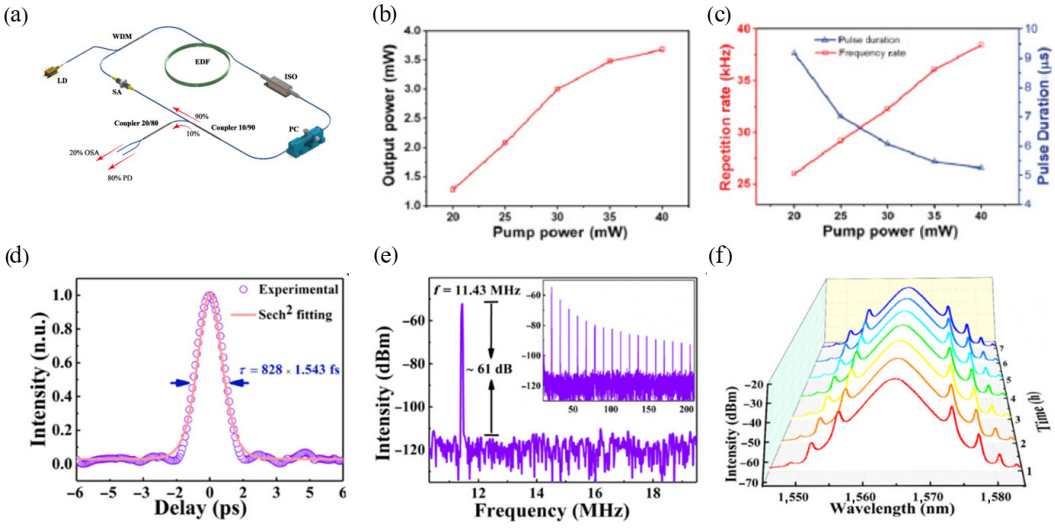

Figure 11 (a) Model diagram of the Er-doped all-fiber ring cavity pulse laser based on b-As$_{0.83}$P$_{0.17}$ SA. (b) Output power variation as a function of the pump power. (c) The relationship between the repetition rate and pulse durations with the pump power. Reproduced with permission from Ref. [46], © Optical Society of America 2019. (d) Autocorrelation trace of the EDF laser based on 2D b-AsP. (e) Radiofrequency of the EDF laser based on the 2D b-AsP SA. (f) Spectral stability of the EDF laser based on the 2D b-AsP SA over time. Reproduced with permission from Ref. [52], © American Chemical Society 2020.

5.4 Silicon photonic microheaters

Silicon photonic microheaters are an important reconstruction technology in silicon photonics that can tune photonic devices without energy loss due to the excellent thermo-optical properties of silicon. Liu et al. reported a nonresonant broadband heater fabricated by a b-AsP nanosheet for tuning silicon optical devices, as shown in Fig. 12(a). The exfoliated b-AsP nanosheet covered on the strip waveguide, followed by applying a voltage to both ends of the nanosheet. Due to the metallic properties of the b-AsP alloy, the carriers locally heated the waveguide through the ohmic heating effect. As shown in Fig. 12(b), the output wavelength shift changes linearly with the heating power, with an efficiency of 0.74 nm/mW. When a 2 V square wave was applied to the microheater, the waveform of the output signal measured by the oscilloscope (Fig. 12(c)) demonstrated a response time of 30 μs and a decay time of 20 μs. Subsequently, a strong correlation with the thickness of the b-AsP nanosheets of the microheater was also demonstrated; the thinner the thickness of the b-AsP flakes, the higher the thermo-optical efficiency. However, it has been a huge challenge thus far to further accelerate the response of silicon photoheaters and to manufacture them on a large scale [54].

5.5 Lithium-ion batteries

A lithium-ion battery is a secondary battery that relies mainly on Li^+ ion intercalation and extraction forth and back between the cathode and anode. 2D materials have huge specific surface areas

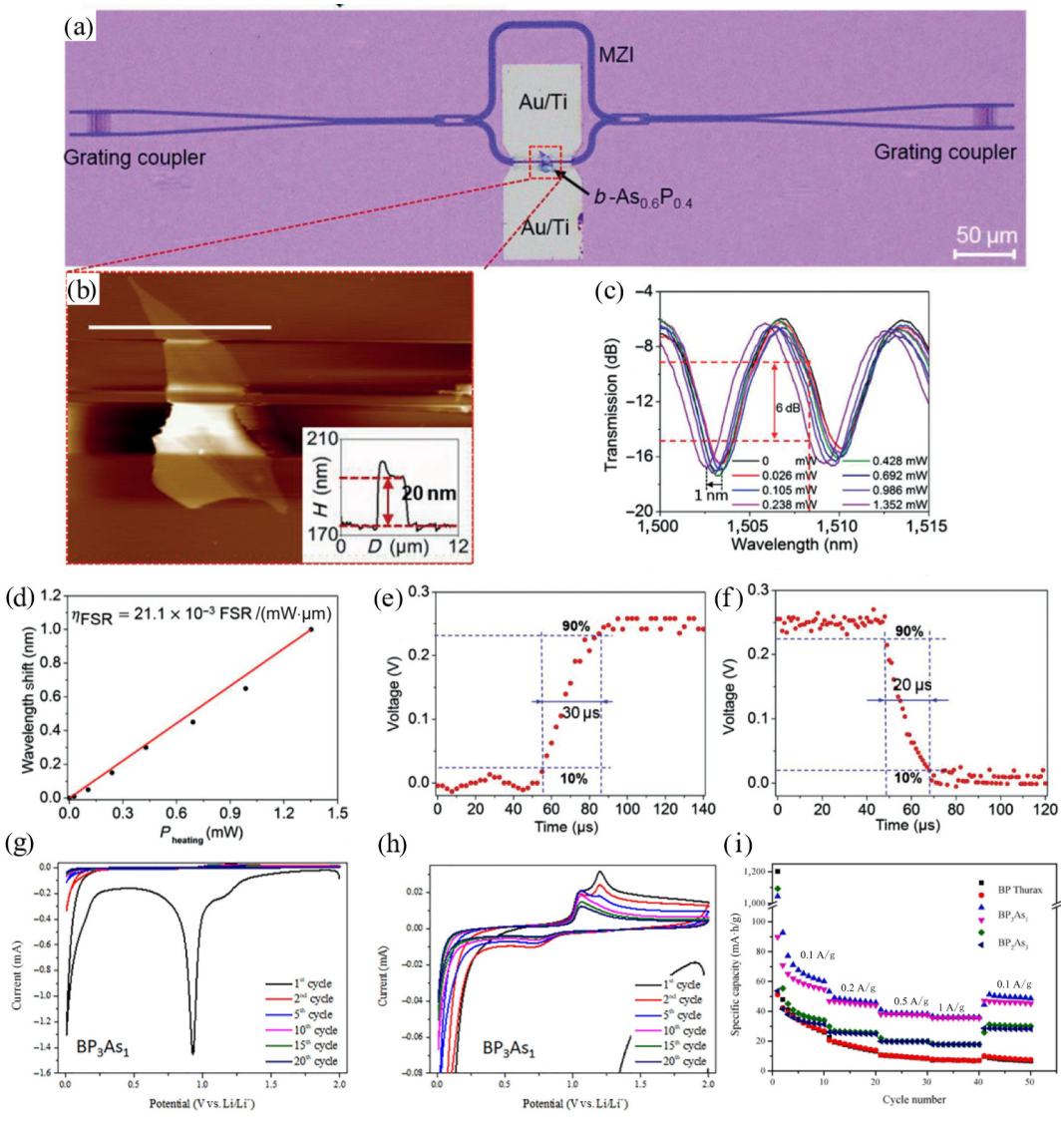

Figure 12 (a) Optical image of the fabricated heater. (b) Atomic force microscopy (AFM) image of the b-AsP covering on the waveguide. The inset is the thickness measurement result. (c) Transmission spectra at different applied electrical powers. (d) The relationship between the wavelength shift and the applied electrical power ($P_{heating}$). (e) and (f) show the waveform of the optical response measured via a sampling oscilloscope. The measured rising time is approximately 30 μs, and the decaying time is approximately 20 μs. Reproduced with permission from Ref. [54], © WILEY-VCH Verlag GmbH & Co. KGaA 2020. (g) CV curves of b-$As_{0.25}P_{0.75}$ at a scan rate of 0.5 mV/s. (h) An enlarged version of the region approximately 1.25 V in (g). (i) Rate capabilities of BP, b-$As_{0.25}P_{0.75}$, and b-$As_{0.6}P_{0.4}$ at various current densities. Reproduced with permission from Ref. [47], © Elsevier B.V. 2019.

with unique surficial properties that are convenient for assembly or modification. Enormous amounts of 2D materials, such as rGO, MoS_2, BN, Ti_3C_2, and BP, have been employed for anode materials of lithium-ion batteries to date [115–119].

In 2020, a study by Jin et al. demonstrated a high-rate and high-capacity lithium storage device by utilizing b-P as the anode active material [47]. Given that the structure of b-AsP is similar to the structure of b-P but with one order of magnitude higher electron mobility of 10,000 $cm^2/(V·s)$ [115], a study on b-AsP as an anode was conducted, including cyclic voltammetry (CV) measurements with redox peaks at 0.5–1.0 V vs. Li/Li^+, which was attributed to the process of Li^+ intercalation (Figs. 12(g) and 12(h)). The peak at 1.0–1.2 V vs. Li/Li^+ was caused by the desertion of Li^+ ions during the reverse scan. The rate capabilities of different arsenic proportions of phosphorus-arsenic alloys at various current densities are shown in Fig. 12(i), featuring a huge loss of specific capacity initially owing to the delithiation of the high lithium phase and the formation of the solid electrolyte interface. Subsequently, an arsenic-phosphorus alloy demonstrated a higher specific capacity than BP, with a Coulombic efficiency approaching 99%, emphasizing the huge application potential of b-AsP alloys in lithium-ion batteries [47].

5.6 Interfacial protection

For practical applications, the material stability in ambient conditions should be carefully studied. It is reported that BP could be degraded after being exposed to air for 3 days, and many bubbles will be formed on the surface of BP. In contrast, it is reported that b-AsP with the similar thickness shows negligible degradation after being exposed to the same air condition for 7 days [54]. The ambient stability of b-AsP is much better than BP, although the surface of b-AsP will still be oxidized to some extent. When stored in ambient air for a long time, an oxidation layer could be formed on the surface of layered b-AsP, resulting in the performance reduction of the devices. To overcome this drawback, some useful strategies have been developed to protect the interface of b-AsP. Liu et al. found that layered b-AsP could be stored in an argon-filled glovebox for one month and the surface still kept very flat [50]. Amani et al. spin-coated a layer of PMMA on the surface of b-AsP and stored it in a nitrogen-filled glovebox, which effectively prevented the degradation of b-AsP [51]. Young et al. deposited a thin layer of Al_2O_3 film on the surface of b-AsP

via the ALD method, which can ensure the ambient stability of b-AsP and the retention of its crystal structure [45]. Yuan et al. fabricated a mid-infrared photodetector with the configuration of sandwiched hBN/b-AsP/hBN structure, which can maintain good performance in ambient conditions for a long time owing to the interfacial protection effect of the upper hBN layer [49].

6 Challenges and perspectives

This review summarizes the recent progress of 2D b-AsP toward structure, synthesis, basic properties, and applications. Alloying BP by arsenic atoms, on the one hand, preserves the special crystal structure and high anisotropic effect of BP and, on the other hand, enhances the tunable range of the band gap and effectively broadens the operational wavelength range in photodetection. The optical response of b-AsP can be as low as approximately 0.15 eV, corresponding to a very long wavelength. Moreover, the long-range composition tuning of b-AsP supplies more flexibility in the manipulation of chemical (stability, reactivity) and physical (electrical and optical) properties. As a monoelemental 2D pnictogen material, BP has been extensively studied in recent years. Other 2D layered pnictogen materials (such as arsenene, antimonene, and bismuthene) are gradually being valued due to their unique properties and great potentials for various devices, such as FETs, photodetectors, batteries, photovoltaic devices, and sensors. However, so far, most of the researches in 2D pnictogen materials were focused on monoelemental pnictogen materials. As a dual-elemental pnictogen material, 2D layered b-AsP undoubtedly paved a new way for 2D pnictogen materials, enriching the category and broadening the application field of 2D pnictogen materials. Until now, 2D b-AsP has been successfully applied in the fields of photodetection, transistors, energy storage, etc.

So far, the research works on monolayer b-AsP have still stagnated at the stage of theoretical calculations. It is still very difficult to obtain large-area, single-layer 2D b-AsP materials with few crystal defects via top-down methods, such as mechanical exfoliation and liquid-phase exfoliation. This is because 2D pnictogen materials with puckered layer structures possess higher interlayer interactions compared to graphene and TMDC materials. In addition, the dual-composition nature of b-AsP further increases the interlayer dispersion interactions. On the other hand, the bottom-up growth of b-AsP is also rarely reported, and the bottom-up growth of monolayer b-AsP has not been realized yet. The CVD method has been considered as one of the most promising routes to realize the growth of b-AsP film with high crystalline quality. However, the lack of suitable precursor material limits the CVD growth of b-AsP. It is hard to break and rearrange the complex bonds of red phosphorus to form the puckered hexagonal orthorhombic crystal phase of b-AsP. The utilization of AsH_3, PH_3, organic phosphine, and organic arsine as sources for the CVD growth of b-AsP has not been explored yet, and suitable catalytic pyrolysis pathways need to be established. For arsenates and phosphates, a feasible experimental procedure is still to be built to overcome their high bond energies and high kinetic energy barriers. Some other deposition technologies also have great potential in the bottom-up synthesis of b-AsP. Molecular beam epitaxy (MBE) equipped with two thermal crack cells can easily generate arsenic atoms and phosphorus atoms, allowing the epitaxial growth of b-AsP crystals on flat substrates. However, the requirements of high vacuum apparatus, expensive effusion cells and suitable substrates limit the development of this method. PLD is also another promising choice for growing b-AsP crystals with a well-controlled elemental ratio. However, for the PLD technique, it is difficult to obtain monolayer b-AsP with high crystal quality because it is hard to avoid the growth of large particles. Overall, there is still plenty of room for researchers in the preparation and applications of monolayer b-AsP materials.

However, the investigation and understanding of b-AsP is just the tip of the iceberg, and there are still many obstacles in the development of 2D b-AsP. The first and foremost difficulty is the large-scale synthesis of 2D b-AsP with controllable thickness and high purity. Current methods to achieve 2D b-AsP focus mainly on mechanical exfoliation and liquid-phase exfoliation of bulk b-AsP. The weakness of mechanical exfoliation is obvious, such as high randomness and low yields, which is far from industrialization. The liquid phase can produce a high yield of 2D b-AsP, and the cost is relatively low and environmentally friendly, making it suitable for catalysis and energy conversion. However, the crystal quality of prepared 2D b-AsP is lower than the crystal quality of mechanical exfoliation, limiting its application in photonics and electronics. In addition, epitaxial growth of BP has been a difficult key problem for a long time. Thus, developing effective wafer-scale and high-quality methods to prepare 2D b-AsP is essential for its practical applications. Large-area film deposition techniques, such as MBD, PLD, ALD, and plasma-enhanced CVD (PECVD), may be an appropriate choice. These results ensure high reproducibility and uniformity and are compatible with the current silicon-based chip fabrication processes.

Although b-AsP has been successfully applied in many fields and some exotic properties of b-AsP have also been experimentally demonstrated, the applications and property engineering of b-AsP alloys are still insufficient. In particular, various theoretical calculations and simulations have predicted fantastic properties of b-AsP, such as superconductivity, low-temperature thermal properties, and mechanical flexibility, requiring further verification and implementation. The high electronic mobility and direct band gap of b-AsP also demonstrate a high potential to act as a highly efficient donor in solar cells. In addition, doping exotic atoms or fabricating defects in b-AsP are also effective ways to adjust the electronic band structures and introduce specific active sites, enabling great potential in the applications of functional electrical and optical devices, sensors, catalysis and lithium and sodium batteries. Notably, the atomic ratio of b-AsP is changeable. Previous theoretical and experimental researches predicted that the As atom ratio in b-AsP can be varied between 0 and 0.83. If the As atomic ratio is higher than 0.83, the commonly used CVT method can only yield gray arsenic phase P-As alloy, rather than b-AsP. Many previous researches have chosen b-$As_{0.83}P_{0.17}$ as a prototype, this is because the b-AsP with an As/P ratio of 0.83:0.17 has the most distinct properties from BP. The b-AsP material with a relatively high proportion of P atoms will depict similar properties to BP, at least to some extent. Therefore, it is reasonable to study the synthesis and characterizations of b-AsP with an As/P ratio of 0.83:0.17. Especially, b-$As_{0.83}P_{0.17}$ exhibits strong light absorption in the wide range of 3.4–7.7 μm, which is favorable for the application of the mid-infrared photodetector. The band gap and optical properties of b-AsP are greatly influenced by the As/P ratio, especially the mid-infrared absorption behavior. Previous studies have shown that with the increase of As concentration, the band gap of b-AsP will decrease and the infrared absorption edge will show a red shift. Moreover, as the concentration of As atoms increases, the characteristic Raman scattering peaks of b-AsP will shift to a low wavenumber, indicating that the increase of the As/P ratio can change the phonon vibration behavior in b-AsP. In short, the wide tunability of the As/P ratio is very beneficial to adjust the properties of b-AsP. However, so far, it is still a lack of comprehensive studies on the tuning of the As/P ratio. For the

future application of b-AsP 2D materials, it is very crucial to realize and make good use of the adjustable characteristics of b-AsP with different atomic ratios. Currently reported crystal phases of arsenic phosphorus alloys are mainly orthorhombic phases with puckered honeycomb structures, which are derived from BP or black arsenic (b-As). Phosphorus or arsenic has diverse allotropes, such as amorphous phosphorus and rhombohedral phosphorus. The crystal phase is an important factor in determining the physical and chemical properties of 2D materials. For instance, rhombohedral arsenic is also a layered crystal and exists in nature, showing semimetallic features with high conductivity. Moreover, as arsenic and phosphorus are in the same group and have similar chemical properties, it is rational that arsenic phosphorus alloys with given atom ratios can be derived from arsenic or phosphorus with different crystal phases. Therefore, rational design and synthesis of 2D arsenic phosphorus alloys with different crystal phases and structures are desirable to fully uncover the intrinsic properties and potentially develop more applications of arsenic phosphorus alloys.

As mentioned above, the challenges of 2D b-AsP also hint at great opportunities for fabricating new conceptual devices and understanding new emerging chemical physics. We hope that this review will provide more inspiration and interest for property research and application developments of 2D b-AsP.

Acknowledgements

This work was supported by the National Key Research and Development Program of China (No. 2017YFA0208200), the Fundamental Research Funds for the Central Universities of China (No. 0205–14380266), the National Natural Science Foundation of China (Nos. 22022505, 21872069, and 22109069), the Natural Science Foundation of Jiangsu Province (No. BK20180008), the Doctoral Innovation and Entrepreneurship Program of Jiangsu Province (No. JSSCBS20210045), and the Shenzhen Fundamental Research Program of Science, Technology and Innovation Commission of Shenzhen Municipality (No. JCYJ20180307155007589).

References

[1] Zhang, S. L.; Guo, S. Y.; Chen, Z. F.; Wang, Y. L.; Gao, H. J.; Gómez-Herrero, J.; Ares, P.; Zamora, F.; Zhu, Z.; Zeng, H. B. Recent progress in 2D group-VA semiconductors: From theory to experiment. *Chem. Soc. Rev.* **2018**, *47*, 982–1021.

[2] Wang, F.; Wang, Z. X.; Yin, L.; Cheng, R. Q.; Wang, J. J.; Wen, Y.; Shifa, T. A.; Wang, F. M.; Zhang, Y.; Zhan, X. Y. et al. 2D library beyond graphene and transition metal dichalcogenides: A focus on photodetection. *Chem. Soc. Rev.* **2018**, *47*, 6296–6341.

[3] Novoselov, K. S.; Geim, A. K.; Morozov, S. V.; Jiang, D.; Zhang, Y.; Dubonos, S. V.; Grigorieva, I. V.; Firsov, A. A. Electric field effect in atomically thin carbon films. *Science* **2004**, *306*, 666–669.

[4] Tao, W.; Kong, N.; Ji, X. Y.; Zhang, Y. P.; Sharma, A.; Ouyang, J.; Qi, B. W.; Wang, J. Q.; Xie, N.; Kang, C. et al. Emerging two-dimensional monoelemental materials (Xenes) for biomedical applications. *Chem. Soc. Rev.* **2019**, *48*, 2891–2912.

[5] Tan, C. L.; Cao, X. H.; Wu, X. J.; He, Q. Y.; Yang, J.; Zhang, X.; Chen, J. Z.; Zhao, W.; Han, S. K.; Nam, G. H. et al. Recent advances in ultrathin two-dimensional nanomaterials. *Chem. Rev.* **2017**, *117*, 6225–6331.

[6] Mannix, A. J.; Kiraly, B.; Hersam, M. C.; Guisinger, N. P. Synthesis and chemistry of elemental 2D materials. *Nat. Rev. Chem.* **2017**, *1*, 0014.

[7] Kong, X. K.; Liu, Q. C.; Zhang, C. L.; Peng, Z. M.; Chen, Q. W. Elemental two-dimensional nanosheets beyond graphene. *Chem. Soc. Rev.* **2017**, *46*, 2127–2157.

[8] Cai, Z. Y.; Liu, B. L.; Zou, X. L.; Cheng, H. M. Chemical vapor deposition growth and applications of two-dimensional materials and their heterostructures. *Chem. Rev.* **2018**, *118*, 6091–6133.

[9] Xie, Z. J.; Duo, Y. H.; Lin, Z. T.; Fan, T. J.; Xing, C. Y.; Yu, L.; Wang, R. H.; Qiu, M.; Zhang, Y. P.; Zhao, Y. H. et al. The rise of 2D Photothermal materials beyond graphene for clean water production. *Adv. Sci.* **2020**, *7*, 1902236.

[10] Chen, P. F.; Li, N.; Chen, X. Z.; Ong, W. J.; Zhao, X. J. The rising star of 2D black phosphorus beyond graphene: Synthesis, properties and electronic applications. *2D Mater.* **2018**, *5*, 014002.

[11] Le Lay, G.; Salomon, E.; De Padova, P.; Layet, J. M.; Angot, T. The rise of elemental two-dimensional materials beyond graphene. *Aust. J. Chem.* **2014**, *67*, 1370–1372.

[12] Geim, A. K.; Novoselov, K. S. The rise of graphene. *Nat. Mater.* **2007**, *6*, 183–191.

[13] Novoselov, K. S.; Jiang, D.; Schedin, F.; Booth, T. J.; Khotkevich, V. V.; Morozov, S. V.; Geim, A. K. Two-dimensional atomic crystals. *Proc. Natl. Acad. Sci. USA* **2005**, *102*, 10451–10453.

[14] Qi, X. L.; Zhang, S. C. Topological insulators and superconductors. *Rev. Mod. Phys.* **2011**, *83*, 1057–1110.

[15] Chhowalla, M.; Shin, H. S.; Eda, G.; Li, L. J.; Loh, K. P.; Zhang, H. The chemistry of two-dimensional layered transition metal dichalcogenide nanosheets. *Nat. Chem.* **2013**, *5*, 263–275.

[16] Geim, A. K.; Grigorieva, I. V. Van der Waals heterostructures. *Nature* **2013**, *499*, 419–425.

[17] Zhang, H. J.; Liu, C. X.; Qi, X. L.; Dai, X.; Fang, Z.; Zhang, S. C. Topological insulators in Bi_2Se_3, Bi_2Te_3 and Sb_2Te_3 with a single Dirac cone on the surface. *Nat. Phys.* **2009**, *5*, 438–442.

[18] Butler, S. Z.; Hollen, S. M.; Cao, L. Y.; Cui, Y.; Gupta, J. A.; Gutiérrez, H. R.; Heinz, T. F.; Hong, S. S.; Huang, J. X.; Ismach, A. F. et al. Progress, challenges, and opportunities in two-dimensional materials beyond graphene. *ACS Nano* **2013**, *7*, 2898–2926.

[19] Xu, M. S.; Liang, T.; Shi, M. M.; Chen, H. Z. Graphene-like two-dimensional materials. *Chem. Rev.* **2013**, *113*, 3766–3798.

[20] Zhang, Y. B.; Tan, Y. W.; Stormer, H. L.; Kim, P. Experimental observation of the quantum Hall effect and Berry's phase in graphene. *Nature* **2005**, *438*, 201–204.

[21] Lopez-Sanchez, O.; Lembke, D.; Kayci, M.; Radenovic, A.; Kis, A. Ultrasensitive photodetectors based on monolayer MoS_2. *Nat. Nanotechnol.* **2013**, *8*, 497–501.

[22] Qiao, J. S.; Kong, X. H.; Hu, Z. X.; Yang, F.; Ji, W. High-mobility transport anisotropy and linear dichroism in few-layer black phosphorus. *Nat. Commun.* **2014**, *5*, 4475.

[23] Li, X. S.; Zhu, Y. W.; Cai, W. W.; Borysiak, M.; Han, B. Y.; Chen, D.; Piner, R. D.; Colombo, L.; Ruoff, R. S. Transfer of large-area graphene films for high-performance transparent conductive electrodes. *Nano Lett.* **2009**, *9*, 4359–4363.

[24] Hsieh, D.; Qian, D.; Wray, L.; Xia, Y.; Hor, Y. S.; Cava, R. J.; Hasan, M. Z. A topological Dirac insulator in a quantum spin Hall phase. *Nature* **2008**, *452*, 970–974.

[25] Zeng, H. L.; Dai, J. F.; Yao, W.; Xiao, D.; Cui, X. D. Valley polarization in MoS_2 monolayers by optical pumping. *Nat. Nanotechnol.* **2012**, *7*, 490–493.

[26] Das Sarma, S.; Adam, S.; Hwang, E. H.; Rossi, E. Electronic transport in two-dimensional graphene. *Rev. Mod. Phys.* **2011**, *83*, 407–470.

[27] Bonaccorso, F.; Colombo, L.; Yu, G. H.; Stoller, M.; Tozzini, V.; Ferrari, A. C.; Ruoff, R. S.; Pellegrini, V. Graphene, related two-dimensional crystals, and hybrid systems for energy conversion and storage. *Science* **2015**, *347*, 1246501.

[28] Reserbat-Plantey, A.; Epstein, I.; Torre, I.; Costa, A. T.; Goncalves, P. A. D.; Mortensen, N. A.; Polini, M.; Song, J. C. W.; Peres, N. M. R.; Koppens, F. H. L. Quantum nanophotonics in two-dimensional materials. *ACS Photonics* **2021**, *8*, 85–101.

[29] Zhao, H.; Guo, Q. S.; Xia, F. N.; Wang, H. Two-dimensional materials for nanophotonics application. *Nanophotonics* **2015**, *4*, 128–142.

[30] Xia, F. N.; Wang, H.; Xiao, D.; Dubey, M.; Ramasubramaniam, A. Two-dimensional material nanophotonics. *Nat. Photonics* **2014**, *8*, 899–907.

[31] Huang, B.; Clark, G.; Navarro-Moratalla, E.; Klein, D. R.; Cheng, R.; Seyler, K. L.; Zhong, D.; Schmidgall, E.; McGuire, M. A.;

Cobden, D. H. et al. Layer-dependent ferromagnetism in a van der Waals crystal down to the monolayer limit. *Nature* **2017**, *546*, 270–273.

[32] Fu, W. Y.; Jiang, L.; van Geest, E. P.; Lima, L. M. C.; Schneider, G. F. Sensing at the surface of graphene field-effect transistors. *Adv. Mater.* **2017**, *29*, 1603610.

[33] Anichini, C.; Czepa, W.; Pakulski, D.; Aliprandi, A.; Ciesielski, A.; Samori, P. Chemical sensing with 2D materials. *Chem. Soc. Rev.* **2018**, *47*, 4860–4908.

[34] Qiu, M.; Ren, W. X.; Jeong, T.; Won, M.; Park, G. Y.; Sang, D. K.; Liu, L. P.; Zhang, H.; Kim, J. S. Omnipotent phosphorene: A next-generation, two-dimensional nanoplatform for multidisciplinary biomedical applications. *Chem. Soc. Rev.* **2018**, *47*, 5588–5601.

[35] Chen, Y.; Tan, C. L.; Zhang, H.; Wang, L. Z. Two-dimensional graphene analogues for biomedical applications. *Chem. Soc. Rev.* **2015**, *44*, 2681–2701.

[36] Li, C. L.; Cao, Q.; Wang, F. Z.; Xiao, Y. Q.; Li, Y. B.; Delaunay, J. J.; Zhu, H. W. Engineering graphene and TMDs based van der Waals heterostructures for photovoltaic and photoelectrochemical solar energy conversion. *Chem. Soc. Rev.* **2018**, *47*, 4981–5037.

[37] Chen, K.; Shi, L. R.; Zhang, Y. F.; Liu, Z. F. Scalable chemical-vapour-deposition growth of three-dimensional graphene materials towards energy-related applications. *Chem. Soc. Rev.* **2018**, *47*, 3018–3036.

[38] Li, L. K.; Yu, Y. J.; Ye, G. J.; Ge, Q. Q.; Ou, X. D.; Wu, H.; Feng, D. L.; Chen, X. H.; Zhang, Y. B. Black phosphorus field-effect transistors. *Nat. Nanotechnol.* **2014**, *9*, 372–377.

[39] Liu, H.; Neal, A. T.; Zhu, Z.; Luo, Z.; Xu, X. F.; Tománek, D.; Ye, P. D. Phosphorene: An unexplored 2D semiconductor with a high hole mobility. *ACS Nano* **2014**, *8*, 4033–4041.

[40] Xia, F. N.; Wang, H.; Jia, Y. C. Rediscovering black phosphorus as an anisotropic layered material for optoelectronics and electronics. *Nat. Commun.* **2014**, *5*, 4458.

[41] Castellanos-Gomez, A.; Vicarelli, L.; Prada, E.; Island, J. O.; Narasimha-Acharya, K. L.; Blanter, S. I.; Groenendijk, D. J.; Buscema, M.; Steele, G. A.; Alvarez, J. V. et al. Isolation and characterization of few-layer black phosphorus. *2D Mater.* **2014**, *1*, 025001.

[42] Buscema, M.; Groenendijk, D. J.; Blanter, S. I.; Steele, G. A.; van der Zant, H. S. J.; Castellanos-Gomez, A. Fast and broadband photoresponse of few-layer black phosphorus field-effect transistors. *Nano Lett.* **2014**, *14*, 3347–3352.

[43] Rodin, A. S.; Carvalho, A.; Castro Neto, A. H. Strain-induced gap modification in black phosphorus. *Phys. Rev. Lett.* **2014**, *112*, 176801.

[44] Chen, Y. B.; Chen, C. Y.; Kealhofer, R.; Liu, H. L.; Yuan, Z. Q.; Jiang, L. L.; Suh, J.; Park, J.; Ko, C.; Choe, H. S. et al. Black arsenic: A layered semiconductor with extreme in-plane anisotropy. *Adv. Mater.* **2018**, *30*, 1800754.

[45] Young, E. P.; Park, J.; Bai, T. Y.; Choi, C.; DeBlock, R. H.; Lange, M.; Poust, S.; Tice, J.; Cheung, C.; Dunn, B. S. et al. Wafer-scale black arsenic-phosphorus thin-film synthesis validated with density functional perturbation theory predictions. *ACS Appl. Nano Mater.* **2018**, *1*, 4737–4745.

[46] Shi, X. Y.; Wang, T.; Wang, J.; Xu, Y. J.; Yang, Z. Y.; Yu, Q.; Wu, J.; Zhang, K.; Zhou, P. Synthesis of black arsenic-phosphorus and its application for Er-doped fiber ultrashort laser generation. *Opt. Mater. Express* **2019**, *9*, 2348–2357.

[47] Luxa, J.; Bouša, D.; Zoller, F.; Fattakhova-Rohlfing, D.; Sofer, Z. Black phosphorus-arsenic alloys for lithium ion batteries. *FlatChem* **2020**, *19*, 100143.

[48] Long, M. S.; Gao, A. Y.; Wang, P.; Xia, H.; Ott, C.; Pan, C.; Fu, Y. J.; Liu, E. F.; Chen, X. S.; Lu, W. et al. Room temperature high-detectivity mid-infrared photodetectors based on black arsenic phosphorus. *Sci. Adv.* **2017**, *3*, e1700589.

[49] Yuan, S. F.; Shen, C. F.; Deng, B. C.; Chen, X. L.; Guo, Q. S.; Ma, Y. Q.; Abbas, A.; Liu, B. L.; Haiges, R.; Ott, C. et al. Air-stable room-temperature mid-infrared photodetectors based on hBN/Black arsenic phosphorus/hBN heterostructures. *Nano Lett.* **2018**, *18*, 3172–3179.

[50] Liu, B. L.; Köpf, M.; Abbas, A. N.; Wang, X. M.; Guo, Q. S.; Jia, Y. C.; Xia, F. N.; Weihrich, R.; Bachhuber, F.; Pielnhofer, F. et al. Black arsenic-phosphorus: Layered anisotropic infrared semiconductors with highly tunable compositions and properties. *Adv. Mater.* **2015**, *27*, 4423–4429.

[51] Amani, M.; Regan, E.; Bullock, J.; Ahn, G. H.; Javey, A. Mid-wave infrared photoconductors based on black phosphorus-arsenic alloys. *ACS Nano* **2017**, *11*, 11724–11731.

[52] Shu, Y. Q.; Guo, J.; Fan, T. J.; Xu, Y. J.; Guo, P. L.; Wang, Z. H.; Wu, L. M.; Ge, Y. Q.; Lin, Z. T.; Ma, D. T. et al. Two-dimensional black arsenic phosphorus for ultrafast photonics in near- and mid-infrared regimes. *ACS Appl. Mater. Interfaces* **2020**, *12*, 46509–46518.

[53] Karki, B.; Rajapakse, M.; Sumanasekera, G. U.; Jasinski, J. B. Structural and thermoelectric properties of black arsenic-phosphorus. *ACS Appl. Energy Mater.* **2020**, *3*, 8543–8551.

[54] Liu, Y. J.; Wang, H. D.; Wang, S.; Wang, Y. J.; Wang, Y. Z.; Guo, Z. N.; Xiao, S. M.; Yao, Y.; Song, Q. H.; Zhang, H. et al. Highly efficient silicon photonic microheater based on black arsenic-phosphorus. *Adv. Opt. Mater.* **2020**, *8*, 1901526.

[55] Yu, L.; Zhu, Z.; Gao, A. Y.; Wang, J. Z.; Miao, F.; Shi, Y.; Wang, X. M. Electrically tunable optical properties of few-layer black arsenic phosphorus. *Nanotechnology* **2018**, *29*, 484001.

[56] Zhou, W. H.; Zhang, S. L.; Wang, Y. Y.; Guo, S. Y.; Qu, H. Z.; Bai, P. X.; Li, Z.; Zeng, H. B. Anisotropic in-plane ballistic transport in monolayer black arsenic-phosphorus FETs. *Adv. Electron. Mater.* **2020**, *6*, 1901281.

[57] Xie, M. Q.; Zhang, S. L.; Cai, B.; Huang, Y.; Zou, Y. S.; Guo, B.; Gu, Y.; Zeng, H. B. A promising two-dimensional solar cell donor: Black arsenic-phosphorus monolayer with 1.54 eV direct bandgap and mobility exceeding 14,000 $cm^2/(V·s)$. *Nano Energy* **2016**, *28*, 433–439.

[58] Osters, O.; Nilges, T.; Bachhuber, F.; Pielnhofer, F.; Weihrich, R.; Schoneich, M.; Schmidt, P. Synthesis and identification of metastable compounds: Black arsenic-science or fiction? *Angew. Chem., Int. Ed.* **2012**, *51*, 2994–2997.

[59] Zhu, Z.; Guan, J.; Tománek, D. Structural transition in layered $As_{1-x}P_x$ compounds: A computational study. *Nano Lett.* **2015**, *15*, 6042–6046.

[60] Bouša, D.; Otyepková, E.; Lazar, P.; Otyepka, M.; Sofer, Z. Surface energy of black phosphorus alloys with arsenic. *ChemNanoMat* **2020**, *6*, 821–826.

[61] Du, H. W.; Lin, X.; Xu, Z. M.; Chu, D. W. Recent developments in black phosphorus transistors. *J. Mater. Chem. C* **2015**, *3*, 8760–8775.

[62] Lu, J. P.; Yang, J.; Carvalho, A.; Liu, H. W.; Lu, Y. R.; Sow, C. H. Light–matter interactions in phosphorene. *Acc. Chem. Res.* **2016**, *49*, 1806–1815.

[63] Rudenko, A. N.; Katsnelson, M. I. Quasiparticle band structure and tight-binding model for single- and bilayer black phosphorus. *Phys. Rev. B* **2014**, *89*, 201408(R).

[64] Jamdagni, P.; Thakur, A.; Kumar, A.; Ahluwalia, P. K.; Pandey, R. Two dimensional allotropes of arsenene with a wide range of high and anisotropic carrier mobility. *Phys. Chem. Chem. Phys.* **2018**, *20*, 29939–29950.

[65] Zhang, P.; Ma, J. Z.; Ishida, Y.; Zhao, L. X.; Xu, Q. N.; Lv, B. Q.; Yaji, K.; Chen, G. F.; Weng, H. M.; Dai, X. et al. Topologically entangled Rashba-split Shockley states on the surface of grey arsenic. *Phys. Rev. Lett.* **2017**, *118*, 046802.

[66] Zhang, S. L.; Yan, Z.; Li, Y. F.; Chen, Z. F.; Zeng, H. B. Atomically thin arsenene and antimonene: Semimetal-semiconductor and indirect-direct band-gap transitions. *Angew. Chem., Int. Ed.* **2015**, *54*, 3112–3115.

[67] Greaves, G. N.; Elliott, S. R.; Davis, E. A. Amorphous arsenic. *Adv. Phys.* **1979**, *28*, 49–141.

[68] Luo, K.; Chen, S. Y.; Duan, C. G. Indirect-direct band gap transition of two-dimensional arsenic layered semiconductors-cousins of black phosphorus. *Sci. China Phys. Mech. Astron.* **2015**, *58*, 87301.

[69] Tang, J. P.; Xiao, W. Z.; Wang, L. L. Stability and electronic

structure of two-dimensional arsenic phosphide monolayer. *Mater. Sci. Eng. :B* **2018**, *228*, 206–212.
[70] Li, L. L.; Bacaksiz, C.; Nakhaee, M.; Pentcheva, R.; Peeters, F. M.; Yagmurcukardes, M. Single-layer Janus black arsenic-phosphorus (b-AsP): Optical dichroism, anisotropic vibrational, thermal, and elastic properties. *Phys. Rev. B* **2020**, *101*, 134102.
[71] Shirotani, I.; Kawamura, H.; Tsuburaya, K.; Tachikawa, K. Superconductivity of phosphorus and phosphorus-arsenic alloy under high pressures. *Jpn. J. Appl. Phys.* **1987**, *26*, 921–922.
[72] Shirotani, I.; Shiba, S.; Takemura, K.; Shimomura, O.; Yagi, T. Pressure-induced phase transitions of phosphorus-arsenic alloys. *Physica B:Condens. Matter* **1993**, *190*, 169–176.
[73] Shirotani, I.; Mikami, J.; Adachi, T.; Katayama, Y.; Tsuji, K.; Kawamura, H.; Shimomura, O.; Nakajima, T. Phase transitions and superconductivity of black phosphorus and phosphorus-arsenic alloys at low temperatures and high pressures. *Phys. Rev. B* **1994**, *50*, 16274–16278.
[74] Nilges, T.; Kersting, M.; Pfeifer, T. A fast low-pressure transport route to large black phosphorus single crystals. *J. Solid State Chem.* **2008**, *181*, 1707–1711.
[75] Köpf, M.; Eckstein, N.; Pfister, D.; Grotz, C.; Krüger, I.; Greiwe, M.; Hansen, T.; Kohlmann, H.; Nilges, T. Access and *in situ* growth of phosphorene-precursor black phosphorus. *J. Cryst. Growth* **2014**, *406*, 6–10.
[76] Wang, Q. H.; Kalantar-Zadeh, K.; Kis, A.; Coleman, J. N.; Strano, M. S. Electronics and optoelectronics of two-dimensional transition metal dichalcogenides. *Nat. Nanotechnol.* **2012**, *7*, 699–712.
[77] Coleman, J. N.; Lotya, M.; O'Neill, A.; Bergin, S. D.; King, P. J.; Khan, U.; Young, K.; Gaucher, A.; De, S.; Smith, R. J. et al. Two-dimensional nanosheets produced by liquid exfoliation of layered materials. *Science* **2011**, *331*, 568–571.
[78] Shu, Y. Q.; Li, J. Q.; Wu, L. M.; Lin, Z. T.; Ma, D. T. Mode-locked pulse generation based on black arsenic phosphorus in erbium-doped fiber lasers. In *Proceedings of the IEEE 5th Optoelectronics Global Conference*, Shenzhen, China, 2020, pp 155–157.
[79] Hernandez, Y.; Nicolosi, V.; Lotya, M.; Blighe, F. M.; Sun, Z. Y.; De, S.; McGovern, I. T.; Holland, B.; Byrne, M.; Gun'Ko, Y. K. et al. High-yield production of graphene by liquid-phase exfoliation of graphite. *Nat. Nanotechnol.* **2008**, *3*, 563–568.
[80] Lotya, M.; Hernandez, Y.; King, P. J.; Smith, R. J.; Nicolosi, V.; Karlsson, L. S.; Blighe, F. M.; De, S.; Wang, Z. M.; McGovern, I. T. et al. Liquid phase production of graphene by exfoliation of graphite in surfactant/water solutions. *J. Am. Chem. Soc.* **2009**, *131*, 3611–3620.
[81] Dreyer, D. R.; Park, S.; Bielawski, C. W.; Ruoff, R. S. The chemistry of graphene oxide. *Chem. Soc. Rev.* **2010**, *39*, 228–240.
[82] Erande, M. B.; Pawar, M. S.; Late, D. J. Humidity sensing and photodetection behavior of electrochemically exfoliated atomically thin-layered black phosphorus nanosheets. *ACS Appl. Mater. Interfaces* **2016**, *8*, 11548–11556.
[83] Ambrosi, A.; Sofer, Z.; Pumera, M. Electrochemical exfoliation of layered black phosphorus into phosphorene. *Angew. Chem., Int. Ed.* **2017**, *56*, 10443–10445.
[84] Xiao, H.; Zhao, M.; Zhang, J. J.; Ma, X. F.; Zhang, J.; Hu, T. J.; Tang, T.; Jia, J. F.; Wu, H. S. Electrochemical cathode exfoliation of bulky black phosphorus into few-layer phosphorene nanosheets. *Electrochem. Commun.* **2018**, *89*, 10–13.
[85] Li, L.; Zhang, D.; Deng, J. P.; Gou, Y. C.; Fang, J. F. Electrochemical exfoliation of two-dimensional layered black phosphorus and applications. *J. Energy Chem.* **2020**, *49*, 365–374.
[86] Shu, H. B.; Guo, J. Y. Electronic and optical properties of phosphorene-like arsenic phosphorus: A many-body study. *Mater. Res. Express* **2018**, *5*, 036302.
[87] Sun, J.; Lin, N.; Ren, H.; Tang, C.; Yang, L. T.; Zhao, X. The electronic structure, mechanical flexibility and carrier mobility of black arsenic-phosphorus monolayers: A first principles study. *Phys. Chem. Chem. Phys.* **2016**, *18*, 9779–9787.
[88] Menzel, R.; Lee, A.; Bismarck, A.; Shaffer, M. S. P. Inverse gas chromatography of as-received and modified carbon nanotubes. *Langmuir* **2009**, *25*, 8340–8348.
[89] Brendlé, E.; Dentzer, J.; Papirer, E. Variation of the surface properties of hematite upon heat treatment evidenced by inverse gas chromatography and temperature programmed desorption techniques: Influence of surface impurities and surface reconstruction. *J. Colloid Interf. Sci.* **1998**, *199*, 63–76.
[90] Boudriche, L.; Calvet, R.; Hamdi, B.; Balard, H. Surface properties evolution of attapulgite by IGC analysis as a function of thermal treatment. *Colloids Surf. A:Physicochem. Eng. Aspects* **2012**, *399*, 1–10.
[91] Mohammadi-Jam, S.; Waters, K. E. Inverse gas chromatography applications: A review. *Adv. Colloid Interface Sci.* **2014**, *212*, 21–44.
[92] Bell, L. E. Cooling, heating, generating power, and recovering waste heat with thermoelectric systems. *Science* **2008**, *321*, 1457–1461.
[93] Smith, B.; Vermeersch, B.; Carrete, J.; Ou, E.; Kim, J.; Mingo, N.; Akinwande, D.; Shi, L. Temperature and thickness dependences of the anisotropic in-plane thermal conductivity of black phosphorus. *Adv. Mater.* **2017**, *29*, 1603756.
[94] Sun, Y. J.; Shuai, Z. G.; Wang, D. Lattice thermal conductivity of monolayer AsP from first-principles molecular dynamics. *Phys. Chem. Chem. Phys.* **2018**, *20*, 14024–14030.
[95] Burns, M. J.; Chaikin, P. M. Interaction effects and thermoelectric power in low-temperature hopping. *J. Phys. C:Solid State Phys.* **1985**, *18*, L743.
[96] Kang, Y. L.; Zhang, Q.; Fan, C. Z.; Hu, W. P.; Chen, C.; Zhang, L.; Yu, F. R.; Tian, Y. J.; Xu, B. High pressure synthesis and thermoelectric properties of polycrystalline Bi_2Se_3. *J. Alloys Compd.* **2017**, *700*, 223–227.
[97] Lin, J. M.; Chen, Y. C.; Yang, C. F.; Chen, W. Effect of substrate temperature on the thermoelectric properties of the Sb_2Te_3 thin films deposition by using thermal evaporation method. *J. Nanomater.* **2015**, *2015*, 1.
[98] Todosiciuc, A.; Nicorici, A.; Condrea, E.; Warchulska, J. Electrical properties of lead telluride single crystals doped with Gd. In *International Conference on Semiconductor*, Sinaia, Romania, 2012, pp 269–272.
[99] Kim, S. I.; Bang, J.; An, J.; Hong, S.; Bang, G.; Shin, W. H.; Kim, T. W.; Lee, K. Effect of Br substitution on thermoelectric transport properties in layered $SnSe_2$. *J. Alloys Compd.* **2021**, *868*, 159161.
[100] Zhu, B. B.; Chen, C.; Yao, Z. C.; Chen, J. Y.; Jia, C.; Wang, Z. H.; Tian, R. M.; Tao, L.; Xue, F.; Hng, H. H. Multiple doped ZnO with enhanced thermoelectric properties. *J. Eur. Ceram. Soc.* **2021**, *41*, 4182–4188.
[101] Kim, J.; Lee, J. U.; Lee, J.; Park, H. J.; Lee, Z.; Lee, C.; Cheong, H. Anomalous polarization dependence of Raman scattering and crystallographic orientation of black phosphorus. *Nanoscale* **2015**, *7*, 18708–18715.
[102] Rajapakse, M.; Musa, R.; Abu, U. O.; Karki, B.; Yu, M.; Sumanasekera, G.; Jasinski, J. B. Electrochemical Li intercalation in black phosphorus: *In situ* and *ex situ* studies. *J. Phys. Chem. C* **2020**, *124*, 10710–10718.
[103] Shojaei, F.; Kang, H. S. Electronic structure and carrier mobility of two-dimensional α arsenic phosphide. *J. Phys. Chem. C* **2015**, *119*, 20210–20216.
[104] Argyris, A.; Syvridis, D.; Larger, L.; Annovazzi-Lodi, V.; Colet, P.; Fischer, I.; García-Ojalvo, J.; Mirasso, C. R.; Pesquera, L.; Shore, K. A. Chaos-based communications at high bit rates using commercial fibre-optic links. *Nature* **2005**, *438*, 343–346.
[105] Tang, Y. F.; Zhan, W. D.; Hao, Z. Q.; Li, R. 10 wireless laser transmission technology for biomedical image information transmission. *J. Invest. Med.* **2019**, *67*, A3–A4.
[106] Lin, X. N.; Lu, Z. W.; Dai, W. L.; Liu, B. C.; Zhang, Y. X.; Li, J. Y.; Ye, J. S. Laser engraved nitrogen-doped graphene sensor for the simultaneous determination of Cd(II) and Pb(II). *J. Electroanal. Chem.* **2018**, *828*, 41–49.
[107] Penilla, E. H.; Devia-Cruz, L. F.; Wieg, A. T.; Martinez-Torres, P.; Cuando-Espitia, N.; Sellappan, P.; Kodera, Y.; Aguilar, G.; Garay, J. E. Ultrafast laser welding of ceramics. *Science* **2019**, *365*, 803–808.
[108] Mears, R. J.; Reekie, L.; Jauncey, I. M.; Payne, D. N. Low-noise erbium-doped fibre amplifier operating at 1.54 μm. *Electron. Lett.* **1987**, *23*, 1026–1028.

[109] Desurvire, E.; Simpson, J. R.; Becker, P. C. High-gain erbium-doped traveling-wave fiber amplifier. *Opt. Lett.* **1987**, *12*, 888–890.
[110] Sobon, G.; Sotor, J.; Pasternak, I.; Krajewska, A.; Strupinski, W.; Abramski, K. M. Multilayer graphene-based saturable absorbers with scalable modulation depth for mode-locked Er- and Tm-doped fiber lasers. *Opt. Mater. Express* **2015**, *5*, 2884–2894.
[111] Chen, B. H.; Zhang, X. Y.; Wu, K.; Wang, H.; Wang, J.; Chen, J. P. Q-switched fiber laser based on transition metal dichalcogenides MoS_2, $MoSe_2$, WS_2, and WSe_2. *Opt. Express* **2015**, *23*, 26723–26737.
[112] Mu, H. R.; Wang, Z. T.; Yuan, J.; Xiao, S.; Chen, C. Y.; Chen, Y.; Song, J. C.; Wang, Y. S.; Xue, Y. Z.; Bao, Q. L. et al. Graphene−Bi_2Te_3 heterostructure as saturable absorber for short pulse generation. *ACS Photonics* **2015**, *2*, 832–841.
[113] Liu, J. S.; Li, X. H.; Guo, Y. X.; Qyyum, A.; Shi, Z. J.; Feng, T. C.; Zhang, Y.; Jiang, C. X.; Liu, X. F. $SnSe_2$ nanosheets for subpicosecond harmonic mode-locked pulse generation. *Small* **2019**, *15*, 1902811.
[114] Chu, Z. Z.; Liu, J.; Guo, Z. N.; Zhang, H. 2 μm passively Q-switched laser based on black phosphorus. *Opt. Mater. Express* **2016**, *6*, 2374–2379.
[115] Jin, H. C.; Xin, S.; Chuang, C. H.; Li, W. D.; Wang, H. Y.; Zhu, J.; Xie, H. Y.; Zhang, T. M.; Wan, Y. Y.; Qi, Z. K. et al. Black phosphorus composites with engineered interfaces for high-rate high-capacity lithium storage. *Science* **2020**, *370*, 192–197.
[116] Li, B.; Zhang, D.; Liu, Y.; Yu, Y. X.; Li, S. M.; Yang, S. B. Flexible Ti_3C_2 MXene-lithium film with lamellar structure for ultrastable metallic lithium anodes. *Nano Energy* **2017**, *39*, 654–661.
[117] Lin, D. C.; Liu, Y. Y.; Liang, Z.; Lee, H. W.; Sun, J.; Wang, H. T.; Yan, K.; Xie, J.; Cui, Y. Layered reduced graphene oxide with nanoscale interlayer gaps as a stable host for lithium metal anodes. *Nat. Nanotechnol.* **2016**, *11*, 626–632.
[118] Cha, E.; Patel, M. D.; Park, J.; Hwang, J.; Prasad, V.; Cho, K.; Choi, W. 2D MoS_2 as an efficient protective layer for lithium metal anodes in high-performance Li−S batteries. *Nat. Nanotechnol.* **2018**, *13*, 337–344.
[119] Yan, K.; Lee, H. W.; Gao, T.; Zheng, G. Y.; Yao, H. B.; Wang, H. T.; Lu, Z. D.; Zhou, Y.; Liang, Z.; Liu, Z. F. et al. Ultrathin two-dimensional atomic crystals as stable interfacial layer for improvement of lithium metal anode. *Nano Lett.* **2014**, *14*, 6016–6022.